Performance enhancement of the combined power-refrigeration cycle using a liquid-gas-gas ejector for ocean thermal energy conversion

Ji Zhang [a,b], Zhixiang Zhang [a], Shiqiao Zhou [a], Hongxun Hui [b], Ning Mei [a,c], Han Yuan [a,*]

[a] *Power Engineering, College of Engineering, Ocean University of China, Qingdao 266100, China*
[b] *The State Key Laboratory of Internet of Things for Smart City, University of Macau, Macau, 999078, China*
[c] *College of Mechanical &Electrical Engineering, Qingdao City University, Qingdao 266100, China*

ARTICLE INFO

ABSTRACT

The practical implementation of ocean thermal energy conversion technology faces constraints due to the low temperature differentials, resulting in limited energy conversion efficiency. This research introduces a novel combined power-refrigeration cycle that utilizes a hybrid liquid-gas-gas ejector to amplify the conversion efficiency. The gas extracted from the turbine is employed as auxiliary fluid within the liquid-gas-gas nozzle, effectively countering the low ejection coefficient associated with conventional liquid-gas ejectors. To elucidate the mechanism behind the liquid-gas-gas ejection process involving an ammonia-water-based absorption working fluid, a comprehensive fluid flow model for ejector is developed. This model facilitates the clarification of the non-equilibrium phase transition process occurring within the ejector. Parametric analysis was conducted to assess cycle performance under various operating conditions. The results show the innovative cycle can attain power/refrigeration efficiencies of 1.58 %/17.45 % while maintaining a refrigeration temperature of −18 °C. Performance comparisons indicate that the proposed liquid-gas-gas ejector based cycle reduces the minimum refrigeration temperature by 20.5 % in contrast to the cycle employing only the liquid-gas ejector, all while preserving power output. Furthermore, despite a mere 26 °C temperature difference, the refrigeration capacity of this cycle significantly outperforms those operating at greater temperature differentials. These findings demonstrate a substantial enhancement in the refrigeration and power capabilities of ocean thermal energy conversion.

1. Introduction

Ocean thermal energy refers to the heat energy resulting from the temperature difference between the ocean's surface and its depths, representing a significant form of ocean energy. The International Energy Agency reports that ocean thermal energy conversion (OTEC) has a theoretical potential of approximately 10,000 TWh/year, which is 1.5 times greater than the energy reserves on land [1]. OTEC possesses substantial reserves and offers stable energy quality, rendering it a highly promising renewable energy source [2]. Nevertheless, the temperature difference between the ocean's surface and its depths is merely around 20–28 °C [3]. The low conversion efficiency of the traditional Rankine cycle, driven by such a small temperature difference, hinders the practical application of OTEC technology. Therefore, minimizing internal thermal losses and optimizing external thermal output are crucial research areas for enhancing OTEC efficiency.

Extensive research has been conducted to enhance the OTEC efficiency. In earlier studies, Rankine cycles [4], Kalina cycles [5], and Uehara cycles [6] are widely adopted; however, their efficiency is relatively low, typically hovering around 3–4 %. To mitigate pressure energy losses in high-pressure solutions, researchers have conducted studies on the OTEC thermal cycle employing ejector theory as a basis. The OTEC ejector cycle, exemplified by ejector absorption technology, employs high-pressure solution to expel low-pressure steam at the expansion turbine outlet. Consequently, it recovers the pressure energy of the high-pressure solution, diminishes the back pressure of the expansion turbine, enhances the functional power of the turbine, and improves the thermal-to-power efficiency of the OTEC cycle [7]. Furthermore, by employing ejectors to establish high, medium, and low pressure conditions, it becomes possible to achieve heat absorption and rejection of the working fluid under varying temperature and pressure conditions. This enables the simultaneous production of cooling and power within a single thermal system, leading to a substantial

Nomenclature

A	Cross-sectional area,m^2
a	Sound velocity,m/s
a_l	Thermal diffusivity,m^2/s
c_p	Specific heat capacity,kJ/kg
D	Diameter, m
E	Exergy, kJ
F	Lateral area, m^2
f	Friction factor
h	Specific enthalpy,kJ/kg
$\dot{I}$	Exergy loss rate, kW
J	Nucleation rate,$m^{-3}s^{-1}$
h_{lv}	Latent heat of vaporization,kJ/(kg·K)
K_l	Mass diffusion coefficient,m^2/s
l	Length, m
M	Molecular mass
$\dot{m}$	Mass flow rate,kg/s
p	Pressure,Pa
$\dot{Q}$	Heat flow rate, kW/kg
q	Latent heat of phase transition,kJ/(kg·K)
R	Gas constant
r	Radius,m
S	Saturation ratio
s	Specific entropy,kJ/(kg·K)
T	Temperature,K
t	Time,s
v	Specific volume,m^3/kg
W	Output power, kW
w	Velocity,m/s
x	Dryness
Z	Frictional forces, N

Greek symbols

α	Heat transfer coefficient,W/(m^2·K)
μ	Kinematic viscosity, m^2/s
ρ	Density,kg/m^3
χ	Ammonia mass fraction
Π	Momentum transfer rate,kg/(m·s)
Γ	Mass transfer rate,kg/s
σ	Surface tension,N/m
η	Efficiency

Subscripts

α	Primary working fluid
β	Auxiliary working fluid
γ	The ejected fluid
l	Liquid phase
g	Gas phase
f	Auxiliary nozzle
s	Isentropic
p	Isobaric
x	Component
in	Inlet
out	Outlet
int	Interface
mix	Mixed phase
hot	Warm seawater
$cold$	Cold seawater
A	Absorber
C	Condenser
E	Evaporator
G	Generator
P	Pump
R	Reheater
T	Turbine

enhancement in overall utilization efficiency [8]. The ejector absorption cycle has emerged as a significant research direction within the field of OTEC cycle theory. Yuan et al. [9] introduced a single-stage injection OTEC cycle that utilizes injection absorption to recover the pressure energy from a dilute ammonia solution. Subsequent experimental verification was conducted. This cycle achieves a theoretical efficiency of 5 %, surpassing that of the Uehara cycle. Subsequently, Jung-In Yoon et al. [10] carried out further investigations based on the aforementioned research, providing evidence that the implementation of liquid–gas injection can enhance the efficiency of the organic Rankine OTEC cycle by 38 %. Xue et al. [11] conducted theoretical research on the ammonia-water absorption double-stage ejection OTEC cycle and showcased performance improvements achieved with a 10 kPa ejection pressure reduction. However, the OTEC cycle technology, designed for power generation purposes, suffers from drawbacks such as low conversion efficiency and a limited range of thermal outputs [12]. Consequently, this leads to high generation costs and challenges in commercialization, thereby significantly impeding the industrial application of OTEC technology.

The development of a novel OTEC ejector cycle theory, capable of satisfying the comprehensive requirements for electricity, refrigeration, and desalination in tropical regions, while enhancing the overall energy efficiency of temperature difference conversion [13], has emerged as a pivotal breakthrough in contemporary OTEC technology [14]. Researchers have undertaken investigations on OTEC ejector power-refrigeration cycles, including double-stage ejector [15], solar-assisted ejector refrigeration [16], and extraction-ejection refrigeration [17]. These studies aim to diminish the cycle's requirement for cold sources

and enhance its operational conditions, thereby attaining refrigeration capabilities below −18 °C. In conclusion, OTEC absorption-based ejector power cycles have emerged as a prominent research focus in the field of ocean thermal energy conversion theory. Ejector technology, as a crucial process for attaining pressure recovery and enabling low-temperature refrigeration, plays a pivotal role in augmenting the conversion efficiency of ocean thermal energy. However, present OTEC research primarily emphasizes the development of thermal cycles, neglecting in-depth investigations into the mechanisms of ammonia-water liquid–gas ejectors. The ejectors employing typical absorbent working fluids such as ammonia solution entails an exceedingly intricate operational process, manifested by the desorption of the ammonia solution within the injector nozzle under a rapid pressure drop, as well as the non-equilibrium phase transitions of ammonia solution, ammonia gas, and water vapor within the mixing chamber. Consequently, it holds great significance to conduct further theoretical investigations into the underlying principles of advanced ejection mechanism.

The primary research approaches for two-phase ejection flow issues comprise theoretical modeling, numerical simulation [18], and experimental analysis [19]. Among these, theoretical modeling provides the most accurate representation of the ejection mechanism. The initial ejection theory model [20] simplified the two-phase injection process as an instantaneous equilibrium process of phase change. However, this model fails to capture the influence of non-equilibrium relaxation phase change on the flow, leading to considerable discrepancies in the calculation results, particularly in high-speed ejectors. Banasiak [21] introduced an enhanced delayed equilibrium model. This model elucidates the mechanism of non-equilibrium two-phase fluid behavior for pure

working fluids by establishing the connection between the condensation-liquefaction rate and the axial flow velocity of the injector, using the gasification index as the key parameter. Subsequently, this theory was employed to forecast and assess the performance of commercial jet refrigeration cycles, and it exhibited favorable predictive outcomes. However, significant differences exist between the phase change driving forces of ammonia-water working fluid and pure working fluid. Additionally, the desorption-absorption process is challenging to depict using classical condensation-evaporation models. Furthermore, the non-equilibrium attributes of phase change cannot be disregarded due to the high-speed flow occurring in the mainstream nozzle and premixing region. These factors significantly influence the phase change laws of ammonia-water two-phase ejection flow. However, the aforementioned factors are seldom considered in current ejector studies.

In conclusion, the present utilization efficiency of existing OTEC technology requires enhancement, and there exists a lack of comprehensive understanding regarding the liquid/gas ejection mechanism within absorption working mediums. To tackle these challenges, this paper predominantly undertook the following innovative research initiatives: Firstly, a novel refrigeration-power combined cycle for OTEC is proposed. This cycle introduces a two-phase mixture ejection method that converts liquid–gas ejection into liquid–gas-gas ejection. The cycle employs high-pressure dilute ammonia water as the primary working fluid for the ejector, while utilizing turbine intermediate extraction-gas to enhance the ejection ability. Secondly, the research established a comprehensive ejector model to describe the non-equilibrium phase change process of the binary absorption working medium (ammonia-water mixture) inside the hybrid nozzle injector. This is achieved by employing energy, momentum, mass conservation equations, state equations, and chemical reaction kinetic equations. The analysis aims to clarify the flow and phase change characteristics of the ammonia-water two-phase mixture ejection and determine the performance of the hybrid nozzle ejector. Finally, the refrigeration and power performance of the new OTEC combined cycle is analyzed under various operation conditions. The research findings of this study are anticipated to offer theoretical and practical guidance for the advancement of OTEC's thermodynamic cycle principles.
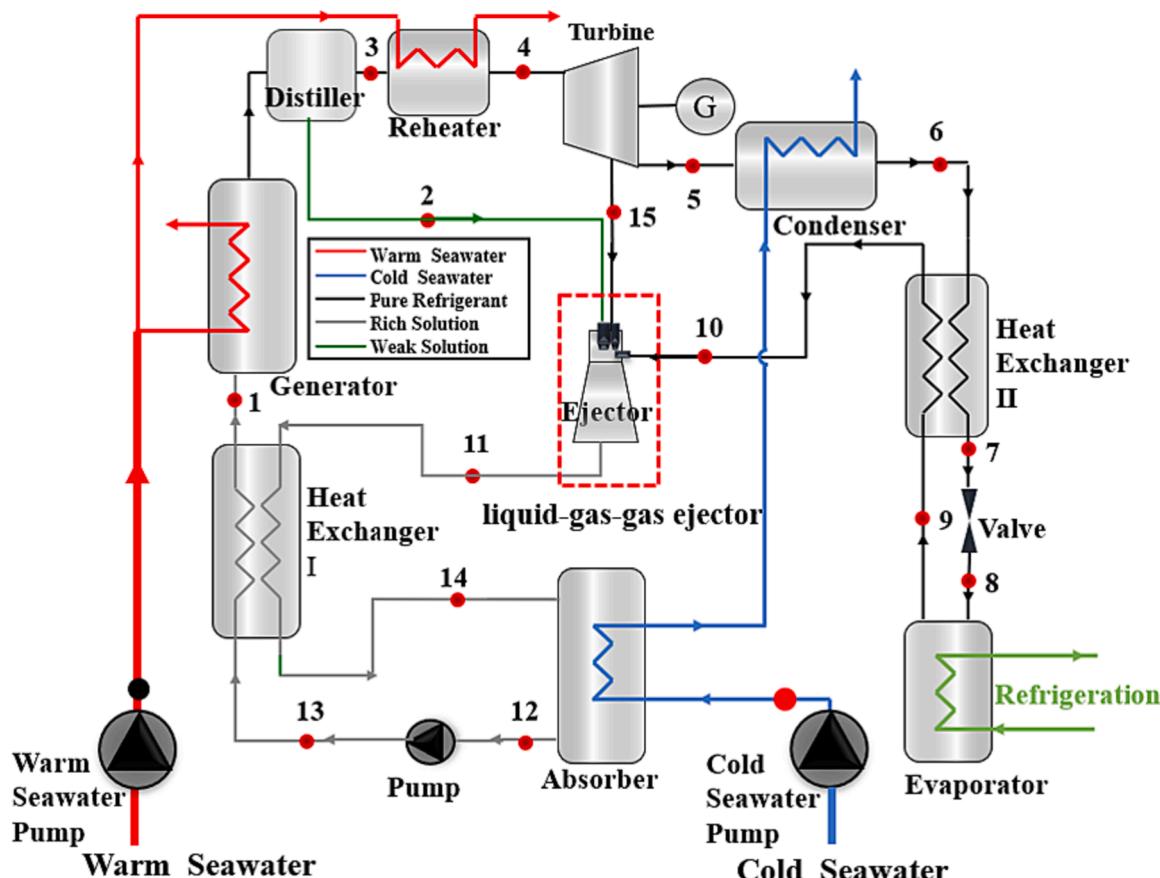
2. Theoretical study

This paper introduces a novel OTEC cycle that employs liquid-gas-gas nozzles and establishes a comprehensive full-channel flow model for a binary working fluid ejector. Accordingly, this section initiates by exploring the proposed OTEC cycle. Subsequently, the cycle model and ejector model are detailed, culminating in the presentation of the model's solution strategy.

2.1. Cycle description

Fig. 1 illustrates the combined power and refrigeration absorption cycle utilizing the hybrid nozzle ejector. The cycle comprises a generator, a distillation unit, a reheater, a turbine, a condenser, a working medium pump, an evaporator, a hybrid nozzle ejector, an absorber, and two heat exchangers. The generator and reheater utilize warm seawater from the surface for heating, while the absorber is cooled by deep cold seawater. Additionally, the evaporator is connected to cold storage to provide external refrigeration. The cycle can be divided into three subsystems based on its functions: power subsystem, circulation subsystem, and refrigeration subsystem.

Fig. 1. OTEC combined power-refrigeration cycle with the liquid-gas-gas ejector.

(i) The power subsystem comprises a reheater and a turbine. The high-temperature ammonia steam from the distillation unit (point 3) is further heated in the heater, resulting in the generation of superheated ammonia steam (point 4). The turbine is equipped with an extraction port. After the superheated ammonia steam enters the turbine (point 15), the high-temperature and high-pressure ammonia steam flows through this extraction port to the hybrid nozzle ejector. After the turbine performs work, the ammonia steam exits the turbine through the turbine outlet (point 5) and enters the condenser.

(ii) The refrigeration subsystem consists of the condenser, heat exchanger II, throttle valve, and evaporator. The ammonia steam from the turbine (point 5) is directed to the condenser, where it is cooled by low-temperature cold seawater, resulting in the condensation of the steam into liquid ammonia (point 6). Once the liquid ammonia flows into the heat exchanger, it undergoes heat transfer with the ammonia steam (point 9). The temperature of the liquid ammonia decreases (point 7), resulting in low-temperature liquid ammonia. The liquid ammonia is then transformed into low-temperature and low-pressure liquid ammonia through the throttle valve (point 8). This low-temperature and low-pressure liquid ammonia evaporates in the evaporator, providing refrigeration for the external cold output. The ammonia steam from the evaporator (point 9) flows through heat exchanger II, resulting in its transformation into superheated ammonia steam (point 10), which then enters the ejector.

(iii) The circulation subsystem comprises the hybrid nozzle ejector, heat exchanger I, absorber, solution pump, and generator. The working fluid inlet of the mixed nozzle ejector is connected to the liquid outlet of the distillation unit (point 2). The auxiliary working fluid inlet of the ejector is connected to the extraction-gas outlet (point 15). The ejected fluid inlet is connected to the heat exchanger II outlet (point 10). To enhance the ejection ability, it is necessary to extract some gas from the middle of the turbine and introduce it into the ejector as an auxiliary ejector fluid. Following the temperature rise and pressure boost, the gas–liquid mixture (point 11) enters the heat exchanger I, where it undergoes heat exchange with the low-temperature ammonia solution (point 13). The relatively high-temperature and high-pressure gas–liquid mixture is cooled to a relatively high-pressure and low-temperature state (point 14). Meanwhile, the low-temperature ammonia solution in heat exchanger I is heated, resulting in a relatively high-temperature ammonia solution (point 1). Subsequently, the high-pressure and low-temperature gas–liquid mixture enters the absorber, where it is cooled by the deep cold seawater. This cooling process transforms the mixture into low-temperature saturated concentrated ammonia water (point 12). The saturated ammonia water is then pressurized by the solution pump, converting it into low-temperature and high-pressure saturated ammonia water (point 13), which flows back to heat exchanger I. In heat exchanger I, the two inlets are supplied with low-temperature and high-pressure concentrated ammonia water from the solution pump (point 13) and the relatively high-temperature gas–liquid mixture from the ejector (point 11), respectively. After sufficient heat exchange, the regenerator has two outlets. The high-temperature and high-pressure concentrated ammonia solution (point 1) flows into the generator, while the low-temperature and low-pressure ammonia gas–liquid mixture (point 14) flows into the absorber. The heat source for the generator is the surface warm seawater. In the generator, the concentrated ammonia water from the regenerator (point 1) is heated by the surface warm seawater, producing a high-temperature, high-pressure, and high-concentration gas–liquid mixture. This gas–liquid mixture then flows into the distillation unit, generating ammonia steam (point

3) and high-temperature, high-pressure dilute ammonia water, which is directed to the reheater and ejector, respectively.

Fig. 2 depicts the structure diagram of the liquid–gas-gas ejector with a hybrid nozzle. The ejector is a mechanical device designed to combine two high-speed, high-pressure fluid jets with a low-speed, low-pressure fluid without the need for external energy input. It has the capability to mix three different flow rates and pressures into a single fluid. The ejector consists of four sections: the nozzle section, premix chamber, mixing chamber, and diffuser chamber. By introducing the β fluid into the ejector, it can enhance the flow rate of the mainstream fluid and reduce its pressure, thereby facilitating the ejection process.

The internal flow process of the mixed nozzle ejector involves various physical phenomena, including the non-equilibrium flow of the main flow, transonic mixing of the main flow and ejected flow, choked flow, shock waves, and other complex processes. Additionally, the desorption and absorption of the two phases (gas and liquid) occur simultaneously, accompanied by the exchange of momentum, mass, and energy. These factors contribute to the intricate nature of the hybrid nozzle ejector operation. In the theoretical analysis section, emphasis will be placed on the modeling of the physical processes taking place within the ejector. The objective of this analysis is to gain a comprehensive understanding of the fluid flow process. Through the incorporation of fundamental principles encompassing fluid dynamics, heat transfer, and mass transfer, mathematical equations and interconnections will be formulated to depict the pertinent phenomena occurring within the ejector. This approach seeks to offer a more precise and intricate depiction of the ejector's behavior.

2.2. Modelling of the proposed cycle with a liquid-gas-gas ejector

The flow of solution into and out of all components in the cycle adheres to the principles of mass and energy conservation.

For the mass conservation equation:

$$\Delta_{\text{out}}^{\text{in}} \sum \dot{m}_i = 0 \tag{1}$$

$$\Delta_{\text{out}}^{\text{in}} \sum \chi_i \dot{m}_i = 0 \tag{2}$$

Where, $\dot{m}_i$ refers to the mass flow rate of the working medium at each state point of the cycle. Eq. (1) represents the conservation of the working fluid throughout the cycle. χ_i is the mass fraction of the ammonia at state point. Eq. (2) represents the conservation of the ammonia throughout the cycle.

The energy equations of for each device are shown in Table 1.

Performance evaluation model:

Due to the present cycle is a combined power refrigeration cycle, the power coefficient and refrigeration coefficient are used respectively to evaluate the output efficiency of the system.

Power coefficient

$$\eta_{\text{power}} = \frac{\dot{W}_{power}}{\dot{Q}_G + \dot{Q}_R} = \frac{\dot{W}_T - \dot{W}_P}{\dot{Q}_G + \dot{Q}_R} \tag{3}$$

Refrigeration coefficient

$$\eta_{\text{ref}} = \frac{\dot{Q}_E}{\dot{Q}_G + \dot{Q}_R} \tag{4}$$

The exergy of each state point in the cycle can be represented as:

$$\dot{E}_i = (h_i - h(T_0, P_0, \chi_i) - T_0(s_i - s(T_0, P_0, \chi_i)))\dot{m}_i/\dot{m}_1 \tag{5}$$

It is noted that the surface seawater temperature utilized by the OTEC cycle is close to atmospheric temperature, whereas the cold seawater temperature is lower than atmospheric temperature. Consequently, in exergy analysis, the chosen environmental temperature corresponds with the heat source temperature.
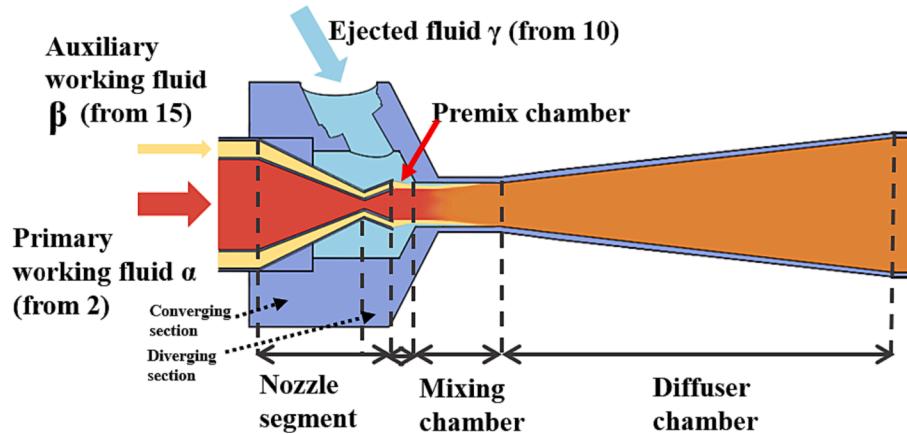
Fig. 2. Diagram of the liquid-gas-gas ejector with the hybrid nozzle.

Table 1
Energy equations of for each device of the OTEC cycle.

Component	Energy equations
Generator and distiller	$\dot{Q}_G = \dot{m_3}h_3 + \dot{m_2}h_2 - \dot{m_1}h_1$
Condenser	$\dot{Q}_C = \dot{m_6}h_6 - \dot{m_5}h_5$
Reheater	$\dot{Q}_R = \dot{m_4}h_4 - \dot{m_3}h_3$
Absorber	$\dot{Q}_A = \dot{m_{14}}h_{14} - \dot{m_{12}}h_{12}$
Evaporator	$\dot{Q}_E = \dot{m_9}h_9 - \dot{m_8}h_8$
Heat exchanger I	$\dot{m_1}(h_1 - h_{13}) = \dot{m_{11}}(h_{14} - h_{11})$
Heat exchanger II	$\dot{m_6}(h_6 - h_7) = \dot{m_9}(h_{10} - h_9)$
Turbine	$\dot{W}_T = \eta_{turbine}(\dot{m_4}h_4 - \dot{m_{15}}h_{15} - \dot{m_5}h_5)$
Pump	$\dot{W}_P = \dfrac{v_{12}\dot{m_{12}}(P_{13} - P_{12})}{\eta_{pump}}$
Throttle valve	$h(T_{14},P_{14},\chi_{14}) = \eta_V h(T_{15},P_{15},\chi_{15})$

where, η_V represents the throttle efficiency.

The exergy loss of each component is defined as follow:

$$\dot{I}_x = \sum \dot{E}x_{in} - \sum \dot{E}x_{out} - \dot{W}_{out} \tag{6}$$

where $\sum \dot{E}x_{in}$ and $\sum \dot{E}x_{out}$ are the exergy inlet and outlet of each component, $\dot{I}_x$ represents the exergy loss rate of component x. $\dot{W}_{out}$ is the useful work output of each component. For pump and turbine, $\dot{W}_{out}$ equals to the work output, while for the heat exchangers of such as Generator, Absorber, $\dot{W}_{out}$ is determined by:

$$\dot{W}_{out} = (1 - \frac{T_{cold}}{T_{hot}})\dot{Q}_x \tag{7}$$

where T_{cold} represents the cold source temperature, T_{hot} represents the heat source temperature, $\dot{Q}_x$ represents the heat flow rate of component x.

2.3. Modelling of the liquid-gas-gas ejector

The working fluid (dilute ammonia water and ammonia gas) flowing through the two nozzles is considered as a closed unidirectional flow channel that is completely isolated from the external environment. The decrease in fluid pressure as the dilute ammonia water flows through the nozzle results in a reduction in the saturation temperature of the ammonia water. Consequently, the ammonia water will reach a boiling point, leading to the generation of a significant amount of ammonia gas,

along with energy and mass transfer between the gas and liquid phases. In this study, a more realistic Delayed Equilibrium Model (DEM) is employed to accurately calculate the process. The premix chamber is modeled using a pseudo one-dimensional approach, where only the fluid parameters at the inlet and outlet sections are calculated. The mixing chamber and diffuser chamber are analyzed using a heat and mass transfer model based on the DEM. The mixing nozzle ejector is treated as a coaxial three-layer annular flow channel using the isobaric mixing model. This comprehensive approach allows for a more accurate representation of the fluid dynamics and heat transfer phenomena in the ejector.

2.3.1. Nozzle segment

This work derives the mass conservation, energy conservation, momentum conservation, and state equations of gas–liquid two-phase flow in the nozzle section of the hybrid nozzle ejector based on the one-dimensional uniform real fluid model proposed by Uuto [22]. The single-flow model makes the calculation more convenient and relies on the following key assumptions:

(1) The fluid in the nozzle is assumed to be one-dimensional and steady. It is assumed that as the fluid passes through the varying cross-sectional area in the nozzle, the mass distribution, state distribution, and chemical distribution of the two-phase flow remain uniform and stable.
(2) It is assumed that there is a motion equilibrium between the liquid and gas phases, and no relative motion occurs between them.
(3) The explicit effects of surface tension and thermal diffusion are neglected in the model.
(4) The energy equation does not consider the effect of turbulent viscous heating, and the turbulence effect is only calculated based on the friction coefficient.
(5) The bubbles are assumed to be spherical, and the interaction between bubbles as well as mutual fusion are not considered.

Then, the governing equations of the nozzle segment are as follows:
Mass conservation equation:

$$\frac{1}{w}\frac{dw}{dl} + \frac{1}{A_i}\frac{dA_i}{dl} + \frac{1}{\rho_i}\frac{d\rho_i}{dl} = \frac{1}{A_i w \rho_i}\frac{d\Gamma_{gl}}{dl} \tag{8}$$

Momentum conservation equation:

$$A\frac{dP}{dl} + Aw\rho\frac{dw}{dl} + f\rho\frac{w^2}{2}\frac{dF}{dl} = 0 \tag{9}$$

Energy conservation equation:

$$\frac{dh_i}{dl} + w\frac{dw}{dl} = (h_g - h_l)\frac{d\Gamma_{gl}}{dl} \tag{10}$$

Equation of state:

$$\frac{d\rho}{dl} - \frac{\partial\rho}{\partial s}\bigg|_P \frac{ds}{dl} - \frac{\partial\rho}{\partial P}\bigg|_S \frac{dP}{dl} = 0 \tag{11}$$

Where,

w: The flow velocity of the working fluid in the nozzle section.
i: Phase state. $i = l$ represents the liquid phase and $i = g$ represents the gas phase.
l: The axial length of the nozzle section.
A: The cross-sectional area of the nozzle section.
f: The friction factor of the nozzle section.
ρ: The density of the working fluid in the nozzle section.
F: The lateral area of the fluid micro-element.
P: The pressure of the working fluid in the nozzle section.
T: The temperature of the working fluid in the nozzle section.
s: The entropy of the working fluid in the nozzle section.
h: The enthalpy of the working fluid in the nozzle section.
Γ_{gl}: The mass transfer rate of phase transition between gas and liquid.

During the calculation, the fluid flow in the ejector is treated as a one-dimensional problem, neglecting the effects of friction and heat dissipation loss.

In the equation of state, the derivative of entropy is replaced by the relationship between specific enthalpy and density in the fundamental equation of thermodynamics.

$$\frac{ds}{dl} = \frac{1}{T}\frac{dh}{dl} - \frac{1}{T\rho}\frac{d\rho}{dl} \tag{12}$$

Using the sound speed equation $\frac{1}{a^2} = \frac{\partial\rho}{\partial P}|S$, the state equation can be rewritten as:

$$\frac{d\rho}{dl} - \frac{\partial\rho}{\partial s}\bigg|_P \frac{ds}{dl} - \frac{1}{a^2}\frac{dP}{dl} = 0 \tag{13}$$

When the fluid is in a single-phase flow, the sound velocity is obtained using the REFPROP 9.11 library. While in the case of two-phase flow, the sonic velocity is determined using the two-phase flow sonic velocity model proposed by [23].

$$a^{-2} = -\frac{1}{v^2}\left(\frac{\partial v}{\partial p}\right)_s = \frac{1}{v^2}\left[x\left(\frac{1}{RT} - \frac{2}{q'} + \frac{Tc_{p,g}}{(q')^2}\right)v_g^2 + (1-x)\frac{Tc_{p,l}}{(q')^2}v_g^2\right] \tag{14}$$

Where a is the sound velocity of two-phase flow, v, v_g, v_l are the specific volume of mixed phase, gas, and liquid phase, respectively, R is the gas constant, x is the dryness, $c_{p,l}$ and $c_{p,g}$ represent the specific heat capacity of liquid phase and the meteorological specific heat capacity respectively, and q' is the latent heat of phase transition, specifically:

$$v = xv_g + (1-x)v_l \tag{15}$$

When the working medium enters the nozzle, its velocity increases and the pressure decreases continuously. The working medium undergoes a transition from an unsaturated solution to a saturated solution. As the saturated solution becomes superheated, the working medium reaches a certain limit and begins to vaporize, resulting in a two-phase flow solution. The gas phase within the two-phase flow solution significantly affects the rate of bubble formation during the boiling, growth, and depressurization processes. Hence, a simple traditional equilibrium phase transition model is insufficient to accurately describe this complex process. To investigate the effect of bubble generation on the bubble formation rate, a non-equilibrium phase transformation model is employed to calculate the state parameters of the working medium in the nozzle. Additionally, a binary solution nucleation model is utilized to calculate the bubble formation rate, gas

volume fraction, and mass fraction in the solution. This approach enhances the accuracy of the calculations. The non-equilibrium model employed in this study incorporates a homogeneous nucleation model for a fully dissolved binary solution. This model considers the impact of surface tension, critical bubble radius, and other factors on the bubble nucleation rate. The calculation formula for Γ_{gl}, as derived in [24], is given below.

$$\Gamma_{gl} = \frac{4}{3}\pi\rho_l Jr_*^2 + 4\pi\rho_l\tau r^2\frac{dr}{dt} \tag{16}$$

where, τ is the dynamic viscosity. r represents the radius of the bubble. Once the bubble is formed, it undergoes continuous growth, and the growth rate is influenced by factors such as pressure, temperature, and concentration. The calculation formula for the growth rate is given as follows [25]:

$$r = \frac{3.7932}{2}\frac{\rho_l C_{p,l}(T_l - T_g)}{\rho_g h_{lv}}\left[1 + |x_{l1} - x_{l2}|^{0.3}\left(\frac{a_l}{K_l}\right)^{0.5}\right]^{-1.1}\sqrt{a_l t} \tag{17}$$

where, h_{lv} is the latent heat of vaporization of liquid, a_l is the thermal diffusion coefficient, K_l is the mass diffusion coefficient.

2.3.2. Auxiliary nozzle segment

The proposed cycle utilizes a single working medium as the auxiliary working fluid. To simplify and improve the accuracy of the calculations, a zero-dimensional isentropic entropy model is adopted.

Mass conservation equation:

$$A_{f,\beta,in}w_{f,\beta,in}\rho_{f,\beta,in} = A_{f,\beta,out}w_{f,\beta,out}\rho_{f,\beta,out} \tag{18}$$

Energy conservation equation:

$$h_{f,\beta,in} + \frac{w_{f,\beta,in}^2}{2} = h_{f,\beta,out} + \frac{w_{f,\beta,out}^2}{2} \tag{19}$$

Isentropic model:

$$s_{f,\beta,in} = \eta_{f,s}s_{f,\beta,out} \tag{20}$$

where, the subscript f represents the fluid flow within the auxiliary nozzle, $\eta_{f,s}$ represent the isentropic efficiency of auxiliary nozzle.

2.3.3. Premix chamber

The main assumptions of the premix chamber model are as follows:

(1) The static pressure of the three air flows at the outlet of the premix chamber is the same.
(2) The fluid flow in the premix chamber is steady-state.
(3) The three air streams form a coaxial three-fluid configuration at the entrance of the mixing chamber. The working fluid flows in the center, the auxiliary working fluid flows in the middle, and the ejected fluid flows in a ring.

Mass conservation equation

$$\begin{aligned}A_{\alpha,in}w_{\alpha,in}\rho_{\alpha,in} &= A_{\alpha,out}w_{\alpha,out}\rho_{\alpha,out} \\ A_{\beta,in}w_{\beta,in}\rho_{\beta,in} &= A_{\beta,out}w_{\beta,out}\rho_{\beta,out} \\ A_{\gamma,in}w_{\gamma,in}\rho_{\gamma,in} &= A_{\gamma,out}w_{\gamma,out}\rho_{\gamma,out}\end{aligned} \tag{21}$$

Energy conservation equation

$$\begin{aligned}h_{\alpha,in} + \frac{w_{\alpha,in}^2}{2} &= h_{\alpha,out} + \frac{w_{\alpha,out}^2}{2} \\ h_{\beta,in} + \frac{w_{\beta,in}^2}{2} &= h_{\beta,out} + \frac{w_{\beta,out}^2}{2} \\ h_{\gamma,in} + \frac{w_{\gamma,in}^2}{2} &= h_{\gamma,out} + \frac{w_{\gamma,out}^2}{2}\end{aligned} \tag{22}$$

Isentropic model

$$\begin{aligned} s_{\alpha,in} &= \eta_y s_{\alpha,out} \\ s_{\beta,in} &= \eta_y s_{\beta,out} \\ s_{\gamma,in} &= \eta_y s_{\gamma,out} \end{aligned} \tag{23}$$

Geometric model

$$A_{\alpha,out} + A_{\beta,out} + A_{\gamma,out} = \frac{\pi}{4} D_{out}^2 \tag{24}$$

At the outlet of the premix chamber, $P_{\alpha,out} = P_{\beta,out} = P_{\gamma,out}$. The subscripts α, β, and γ represent the working fluid, auxiliary working fluid, and ejector fluid, respectively. The subscripts "in" and "out" represent the inlet and outlet of the premix chamber, respectively. D represents the outlet diameter of the premix chamber.

2.3.4. Mixing chamber and diffuser chamber

In this study, the mixing chamber and the diffuser chamber are considered together in the calculations. This is because the mass, momentum, and energy exchange processes are essentially the same in both chambers, with the only difference being the longitudinal cross-sectional area of the flow passage. Geometric equations are incorporated into the equations to account for the change in the longitudinal cross-section area of the diffuser.

When the working medium changes from single-phase flow to gas–liquid two-phase flow in the nozzle, there is not only evaporation driven by nucleation, but also condensation with the change of working medium temperature, pressure and gas phase concentration. Especially when ammonia water is used as the working medium, there is desorption and absorption phenomenon during the ammonia water flow. This phenomenon is essentially a mass transfer process existing in the two-phase flow. To precisely characterize this process, a specialized reaction kinetics-driven non-equilibrium mass transfer model must be established for the ejector. In this study, the double membrane model serves as the non-equilibrium mass transfer model to compute the gas–liquid mass transfer rate between the two-phase flows. For a more accurate portrayal of the internal mass transfer process of ammonia during flow, the chemical reaction kinetic formula of ammonia is incorporated into the mass transfer model.

The following assumptions are made for the mixing chamber and the diffuser chamber:

(1) The working fluid, auxiliary working fluid, and ejected fluid entering the flow channel form a fully coaxial three-fluid annular flow. Any potential conversion between the three annular flows is considered as a conversion of mass, momentum, and energy [26].
(2) The static pressure of the three streams is assumed to be the same.
(3) An infinitely thin boundary layer exists between the three fluids, allowing for the transfer of mass, energy, and momentum between the fluids.
(4) Mass transfer is accounted for by three different mechanisms: condensation transfer, desorption and absorption transfer, and entrainment transfer.

Mass conservation equation

$$A_\alpha \rho_\alpha \frac{dw_\alpha}{dl} + A_\alpha w_\alpha \frac{d\rho_\alpha}{dl} + w_\alpha \rho_\alpha \frac{dA_\alpha}{dl} = -\frac{d\Gamma_c}{dl} - \frac{d\Gamma_{NH_3}}{dl} - \frac{d\Gamma_{\alpha\rightarrow\beta}}{dl} \tag{25}$$

$$A_\beta \rho_\beta \frac{dw_\beta}{dl} + A_\beta w_\beta \frac{d\rho_\beta}{dl} + w_\beta \rho_\beta \frac{dA_\beta}{dl} = \frac{d\Gamma_c}{dl} + \frac{d\Gamma_{NH_3}}{dl} + \frac{d\Gamma_{\alpha\rightarrow\beta}}{dl} + \frac{d\Gamma_c^{'}}{dl} + \frac{d\Gamma_{\gamma\rightarrow\beta}}{dl} \tag{26}$$

$$A_\gamma \rho_\gamma \frac{dw_\gamma}{dl} + A_\gamma w_\gamma \frac{d\rho_\gamma}{dl} + w_\gamma \rho_\gamma \frac{dA_\gamma}{dl} = -\frac{d\Gamma_c^{'}}{dl} - \frac{d\Gamma_{\gamma\rightarrow\beta}}{dl} \tag{27}$$

Momentum conservation equation:

$$A_\alpha \frac{dp}{dl} + A_\alpha w_\alpha \rho_\alpha \frac{dw_\alpha}{dl} = (w_\alpha - w_{int})\left(\frac{d\Gamma_c}{dl} + \frac{d\Gamma_{NH_3}}{dl}\right) + \frac{d\Pi}{dl} \tag{28}$$

$$A_\beta \frac{dp}{dl} + A_\beta w_\beta \rho_\beta \frac{dw_\beta}{dl} = (w_{int} - w_\beta)\frac{d\Gamma_c}{dl} + (w_\alpha - w_\beta)\frac{d\Gamma_{\alpha\rightarrow\beta}}{dl} - \frac{d\Pi}{dl} - \frac{dZ_{f,int}}{dl} + (w_{int}^{'} - w_\beta)\frac{d\Gamma_c^{'}}{dl} + (w_\gamma - w_\beta)\frac{d\Gamma_{\gamma\rightarrow\beta}}{dl} - \frac{d\Pi^{'}}{dl} - \frac{dZ_{f,int}^{'}}{dl} \tag{29}$$

$$A_\gamma \frac{dp}{dl} + A_\gamma w_\gamma \rho_\gamma \frac{dw_\gamma}{dl} = (w_\gamma - w_{int})\frac{d\Gamma_c^{'}}{dl} + \frac{d\Pi^{'}}{dl} - \frac{dZ_{f,w}}{dl} \tag{30}$$

Energy conservation equation

$$A_\alpha w_\alpha^2 \rho_\alpha \frac{dw_\alpha}{dl} + A_\alpha w_\alpha \rho_\alpha \frac{dh_\alpha}{dl} = \left(h_\alpha - h_{int} + 0.5\left(w_\alpha^2 - w_{int}^2\right)\right)\left(\frac{d\Gamma_c}{dl} + \frac{d\Gamma_{NH_3}}{dl}\right) \tag{31}$$

$$A_\beta w_\beta^2 \rho_\beta \frac{dw_\beta}{dl} + A_\beta w_\beta \rho_\beta \frac{dh_\beta}{dl} = \left(h_{int} - h_\beta + 0.5\left(w_{int}^2 - w_\beta^2\right)\right)\frac{d\Gamma_c}{dl} + \left(h_{int}^{'} - h_\beta + 0.5\left(w_{int}^2 - w_\beta^2\right)\right)\frac{d\Gamma_c^{'}}{dl} + \left(h_\alpha - h_\beta + 0.5\left(w_\alpha^2 - w_\beta^2\right)\right)\frac{d\Gamma_{\alpha\rightarrow\beta}}{dl} + \left(h_\gamma - h_\beta + 0.5\left(w_\gamma^2 - w_\beta^2\right)\right) \tag{32}$$

$$A_\gamma w_\gamma^2 \rho_\gamma \frac{dw_\gamma}{dl} + A_\gamma w_\gamma \rho_\gamma \frac{dh_\gamma}{dl} = \left(h_\gamma - h_{int} + 0.5\left(w_{int}^2 - w_\gamma^2\right)\right)\frac{d\Gamma_c^{'}}{dl} \tag{33}$$

State equation:

$$\left(T_\alpha \rho_\alpha - a_\alpha^2 \frac{\partial \rho_\alpha}{\partial s}\Big|_P\right)\frac{dp}{dl} + \rho_\alpha a_\alpha^2 \frac{\partial \rho_\alpha}{\partial s}\Big|_P \frac{dh_\alpha}{dl} - T_\alpha \rho_\alpha a_\alpha^2 \frac{d\rho_\alpha}{dl} = 0 \tag{34}$$

$$\left(T_\beta \rho_\beta - a_\beta^2 \frac{\partial \rho_\beta}{\partial s}\Big|_P\right)\frac{dp}{dl} + \rho_\beta a_\beta^2 \frac{\partial \rho_\beta}{\partial s}\Big|_P \frac{dh_\beta}{dl} - T_\beta \rho_\beta a_\beta^2 \frac{d\rho_\beta}{dl} = 0 \tag{35}$$

$$\left(T_\gamma \rho_\gamma - a_\gamma^2 \frac{\partial \rho_\gamma}{\partial s}\Big|_P\right)\frac{dp}{dl} + \rho_\gamma a_\gamma^2 \frac{\partial \rho_\gamma}{\partial s}\Big|_P \frac{dh_\gamma}{dl} - T_\gamma \rho_\gamma a_\gamma^2 \frac{d\rho_\gamma}{dl} = 0 \tag{36}$$

Geometric model

$$\frac{dA_\alpha}{dl} + \frac{dA_\beta}{dl} + \frac{dA_\gamma}{dl} = \frac{dA}{dl} \tag{37}$$

where, a represents fluid sonic velocity ; Γ_c represents the condensing mass transfer between the working fluid and the auxiliary working fluid, and $\Gamma_c^{'}$ represents the condensing mass transfer between the auxiliary working fluid and the ejected fluid. Γ_{NH_3} is the mass transfer of the desorption and absorption process of the ammonia water. $\Gamma_{\alpha\rightarrow\beta}$ represents the mass transfer resulting from the working fluid being entrained by the auxiliary working fluid, while $\Gamma_{\gamma\rightarrow\beta}$ represents the mass transfer resulting from the ejected fluid being entrained by the auxiliary working fluid. Π and $\Pi^{'}$ represent the momentum transfer differential at the interface between the working fluid and the auxiliary working fluid, and the momentum transfer differential at the interface between the auxiliary working fluid and the ejected fluid, respectively. $Z_{f,int}$, $Z_{f,int}^{'}$ and $Z_{f,w}$ represent the frictional forces between the working fluid and auxiliary working fluid, auxiliary working fluid and ejection fluid, and ejection fluid and wall surface, respectively. The parameters on the interface of the two-phase flow w_{int}, h_{int} are determined according to the condensation direction at the interface.

After obtaining the calculation methods for the parameters in the above equations, Eq. (22)-(34) are combined to establish a system of linear equations.

It is important to note that in the main body of the article, the derivation principles and main forms of the Eq.(25–37) have been retained to maintain simplicity. For the determination of internal parameters and the expression of specific solutions of the equations, please refer to Appendix A for detailed information.

2.4. Solution strategy

The new OTEC cycle and the liquid-gas-gas ejector need to be solved coupled. The cyclic computation was implemented using MATLAB and REFPROP. The calculation process of the OTEC cycle is shown in Fig. 3. The main assumptions of the cycle model are as follows.

(1) All component models in this cycle are assumed to be in steady state.
(2) All heat exchangers are assumed to operate under isobaric conditions, neglecting the pressure drop inside pipes and heat exchangers.
(3) At the outlet of the condenser and absorber, the solution is assumed to be in a saturated state. Similarly, the ammonia vapor at the evaporator outlet and the ammonia water at the absorber outlet are also considered saturated.
(4) Pumps and turbines are characterized by specific isentropic efficiencies, while throttle valves possess defined efficiencies.

The initial parameter settings are listed in Table 2.

The governing equations are solved using MATLAB for the entire flow passage of the ejector. Due to the different nature of the governing equations in the nozzle section, premix chamber, mixing chamber, and diffuser chamber, separate solving strategies are employed for each part. Consequently, the four sections are calculated independently. The schematic diagram illustrating the technical approach for solving the

Table 2
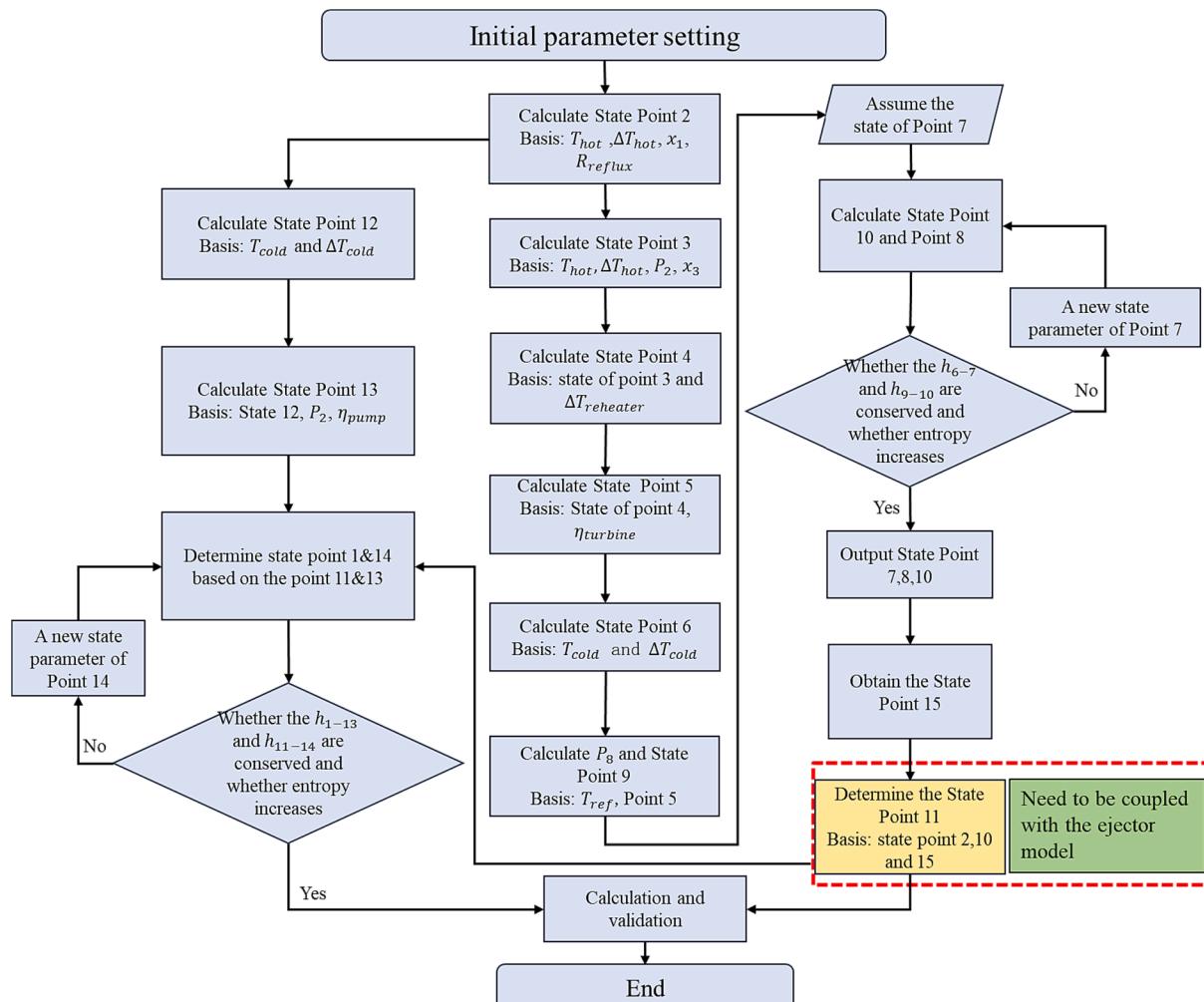Initial parameter settings of the OTEC combined power-refrigeration cycle.

Initial parameter	Value	Unit
Warm seawater temperature/T_{hot}	30	°C
Cold seawater temperature/T_{cold}	4	°C
Heat transfer temperature difference in generator/ΔT_{hot}	3	°C
Heat transfer temperature difference in condenser and absorber/ΔT_{cold}	3	°C
Isentropic efficiency of pump/η_{pump}	85 %	/
Isentropic efficiency of turbine/$\eta_{turbine}$	80 %	/
Superheat of the reheater/$\Delta T_{reheater}$	5	°C
Refrigeration temperature/T_{ref}	−18	°C
Reflux ratio (m₂/m₃)/R_{reflux}	1.5	/
Ammonia mass fraction at point 1/χ_1	85 %	/
Ammonia mass fraction at point 3/χ_3	99.5 %	/
Mass flow at state point 3/m_3	1	kg/s

full channel of the ejector is depicted in Fig. 4.

The diagram of the ejector can be found in Fig. 2. The ejector structure and size can be determined according to Appendix B. In this work, the ejector size is shown in Table 3.

3. Verification methods

In this work, the proposed ejector model and the OTEC cycle need to be verified respectively. The verification methods are shown as follows.

Fig. 3. The calculation process of the OTEC combined power-refrigeration cycle.
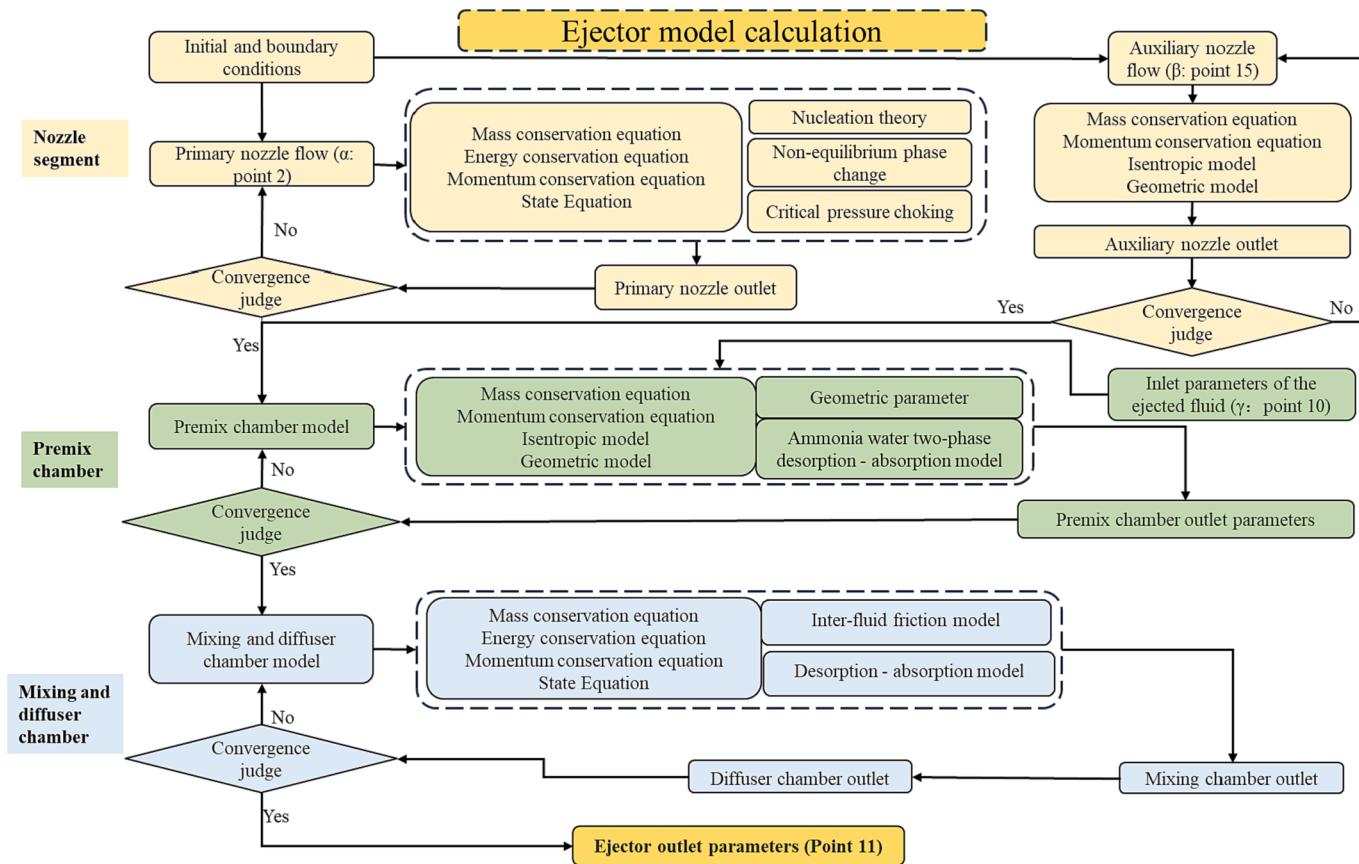
Fig. 4. Calculation flow chart for solving the full channel of the ejector.

Table 3
Structural size of the liquid-gas-gas ejector.

Ejector component	Parameters	Size
Primary fluid nozzle	Inlet radius/m	0.05
	Throat radius/m	0.03
	Outlet radius/m	0.048
	Inclination angle of the wall at the converging section/°	5
	Inclination angle of the wall at the diverging section/°	3
	Nozzle length/m	0.74
Auxiliary fluid nozzle	Inlet radius/m	0.15
	Throat radius/m	0.02
	Outlet radius/m	0.01
	Inclination angle of the wall at the converging section/°	7
	Inclination angle of the wall at the diverging section/°	2
	Nozzle length/m	0.74
Mixing chamber	Premix chamber length/m	0.2
	Chamber radius/m	0.0547
	Mixing chamber length/m	0.235
Diffuser chamber	Length/m	1
	Inclination angle of the wall/°	6

(Note: The inclination of the wall is the sharp angle to the horizontal line) .

3.1. Verification of the ejector model

The validity of the ejector model is confirmed by comparing it with experimental data. It is important to note that the ejector model proposed in this paper is specifically designed to address the challenges associated with heat transfer, mass transfer, and momentum transfer between fluids. As a result, it can be applied to a wide range of processes involving the ejection of ammonia water and ammonia gas. This work selects experimental data from reference [27] for comparison and verification. The experiment employs a liquid–gas standard ejector with ammonia-water as the working medium. The working medium undergoes condensation, entrainment, and desorption-absorption processes in the ejector, which aligns with the applicable scope of the ejector model presented in this paper. This experiment evaluates the performance of the ejector by measuring the pressures of the primary working fluid and the ejected fluid. The comparison between the data calculated using the ejector model presented in this paper and the experimental data is illustrated in Fig. 5. From the figure, it is evident that the calculation model presented in this paper exhibits greater consistency with the experimental data compared to the pressure data calculated in the literature. The average error of the calculation model is less than 10 % under varying mainstream temperature conditions, indicating a high level of accuracy. The reason for this is that the ejector model presented in this paper comprehensively accounts for the entire occurrence process of the flow working medium in the ejector's flow channel. This approach aligns more closely with the actual situation compared to traditional ejector calculation methods (such as the aerodynamic function method, etc.).

3.2. Verification of the proposed cycle

In the verification of cycle rationality, the energy conservation and entropy are verified based on the law of thermodynamics. The detailed verification equations are given below:

(1) Energy balance:

$$\left| \left(\dot{Q}_G + \dot{Q}_R + \dot{Q}_E + \dot{W}_P - \dot{Q}_A - \dot{Q}_C - \dot{W}_T \right)/\dot{Q}_G \right| \langle 0.5\% \tag{38}$$

Fig. 5. Performance verification of the ejector model.

(2) Check whether the ejection process follows the principle of entropy increment:

$$\dot{m}_{11}s_{11} - \dot{m}_2s_2 - \dot{m}_{10}s_{10} - \dot{m}_{15}s_{15} > 0 \tag{39}$$

(3) Check whether the throttling process follows the principle of entropy increment:

$$\dot{m}_8s_8 - \dot{m}_7s_7 > 0 \tag{40}$$

4. Results and discussion

In the OTEC cycle proposed in this paper, which employs hybrid nozzles, the ejector serves as a pivotal component for enhancing system performance. Consequently, this section undertakes an exhaustive analysis of the cyclic calculation outcomes and the ejector's performance. Subsequently, a detailed examination of the key parameters influencing system performance is conducted. Lastly, the enhancement brought about by the proposed cycle in this paper is analyzed through a comparison of its efficiency with that of a previously published cycle, particularly under conditions of low temperature difference.

4.1. Calculation results and analysis of the cycle

The performance of each state point in the system is presented in Table 4, based on the solution strategy and initial parameter setting described in section 2.4. The performance calculation results meet the verification conditions in section 3.2. The results indicate that this cycle can achieve significant refrigeration output. Due to the low refrigeration temperature, the outlet pressure of the evaporator (state point 9) is significantly lower than that of the absorber. The pressure drop in the absorber depends on the concentration and gas content of ammonia flowing into the absorber, given the cold source temperature and the heat transfer temperature difference in the absorber.

The output parameters (point 11) of the ejector are calculated using the governing equation presented in section 2.3. These parameters are then used in the calculation of state points throughout the cycle. Compared to the traditional ejection combined refrigeration-power

Table 4
Results of the OTEC cycle under the initial parameter settings.

State point	Pressure	Temperature	Enthalpy	Entropy	Mass flow rate	Ammonia mass fraction
	kPa	°C	kJ/kg	kJ/(kg*K)	kg/s	
1	776.39	12.1	226.61	1.35	2.50	85.0 %
2	776.39	27.0	207.81	1.38	1.50	75.0 %
3	776.39	22.0	1635.83	5.93	1.00	99.5 %
4	776.39	27.0	1649.94	5.98	1.00	99.5 %
5	553.85	7.9	1615.02	6.01	0.19	99.5 %
6	553.85	7.0	375.69	1.59	0.19	99.5 %
7	553.85	−5.3	319.09	1.38	0.19	99.5 %
8	207.56	−18.0	319.09	1.39	0.19	99.5 %
9	207.56	−18.0	1583.55	6.35	0.19	99.5 %
10	207.56	6.0	1640.15	6.56	0.19	99.5 %
11	470.33	12.6	774.59	3.31	2.50	85.0 %
12	470.33	7.0	209.91	1.28	2.50	85.0 %
13	776.39	7.3	211.30	1.28	2.50	85.0 %
14	470.33	7.7	759.28	3.24	2.50	85.0 %
15	598.36	11.5	1621.10	6.00	0.81	99.5 %

cycle, the cycle is modified to utilize liquid–gas-gas ejection rather than liquid–gas ejection. This modification enables the complete utilization of pressure energy and internal energy in the dilute ammonia solution, leading to an improved energy utilization efficiency within the cycle. The performance of the individual components and the overall system is presented in Table 5. The system demonstrates a power efficiency of 1.58 % and a refrigeration coefficient of 17.45 %, exceeding those of the traditional combined refrigeration-power cycle. A detailed comprehensive analysis of the impact of relevant parameters on the cycle's performance and a comparison with other cycles will be presented in the subsequent section.

Fig. 6 represents the Temperature-Specific entropy diagram of the cycle, depicting the division of the OTEC cycle into positive and reverse cycles. In the diagram, the black, blue, and yellow pathways constitute the positive cycle, facilitating the thermodynamic process of the system. The red cycle signifies the reverse refrigeration cycle. The three fluid streams converge at the ejector, undergoing an irreversible mixing process leading to point 11 (ejector). Subsequently, the fluids are cooled by cold seawater and absorbed in the absorption unit. The crucial role of the ejector becomes evident in enabling the interaction of positive and reverse circulation and the convergence of the three fluid streams.

Fig. 7 illustrates the temperature–pressure and pressure-enthalpy diagrams of the OTEC cycle incorporating a hybrid nozzle. As can be seen from Fig. 6(a), the state of ammonia changes as ammonia does work in the turbine. The intermediate pumping point 15 is positioned between state points 4 and 5, indicating that the working fluid from the ejector can drive both the injector and generate power output. As the superheated ammonia enters the turbine and performs external work, its temperature and superheat decrease. As the ammonia nears the completion of work, its superheat reaches zero, and it begins to liquefy. Subsequently, the temperature and pressure decrease towards the saturation pressure line, with the pressure decreasing at a faster rate. If gas is pumped between points 4 and 5, the corresponding pumping point will be located above the line connecting points 4 and 5. The cycle operates at four primary pressure levels: production pressure (state point 2), evaporator pressure (state point 8), absorption pressure (state point 12), and turbine extraction pressure (state point 15). Fig. 6(b) illustrates that the primary enthalpy change takes place within the heat exchanger. By incorporating a heat exchanger between the generator and the absorbent, the ammonia-rich aqueous solution at state point 1 can be effectively reheated, resulting in a substantial reduction in the heat load on the generator.

Fig. 8 shows the proportion of exergy loss of each component in this cycle. Considering the inclusion of refrigeration functionality in this OTEC cycle, the most substantial exergy loss within the system transpired in the absorber, constituting 40.8 % of the total exergy loss. The generator and evaporator accounted for 14.7 % and 11.7 %, respectively, of the total exergy loss within the system. Owing to its proximity to ambient temperature, the generator exhibits a reduced exergy loss compared to a component possessing comparable power. The evaporator undergoes a gas–liquid two-phase transition, leading to an increased exergy loss despite its lower power requirement. The ejector contributes merely 2.9 % to the overall exergy loss of the system,

underscoring its effectiveness as a kinetic energy conversion unit. This efficiency ensures thorough harnessing of pressure across the system.

4.2. Performance analysis of the liquid-gas-gas ejector

Fig. 9 represents the full channel pressure distribution of three fluids in the ejector with the hybrid nozzle. When the β fluid enters the ejector, it interacts with the mainstream fluid in the premix chamber and mixing chamber. Due to the high speed of the β fluid, it imparts momentum and energy to the mainstream fluid, effectively accelerating its flow. This acceleration of the mainstream fluid allows for a higher flow rate within the ejector. Moreover, the β fluid's entry into the mixing chamber creates a pressure gradient that helps to lower the pressure of the mainstream fluid. As the β fluid expands and mixes with the mainstream fluid, it induces a decrease in pressure, creating a favorable pressure difference for the ejection process. This pressure reduction enables the ejected fluid to be efficiently entrained and entrapped by the mainstream fluid, facilitating the desired flow and mixing patterns. By utilizing the β fluid in this manner, the ejector can achieve improved fluid dynamics and better ejection performance. The increased flow rate and reduced pressure of the mainstream fluid contribute to enhanced efficiency and effectiveness of the ejector in applications such as OTEC cycles.

Fig. 10 shows the parameter variation of the ejected fluid under different pressure inlet in the ejector mixing section. Fig. 10 (a) and (b) and (c) show the flow velocity and area of the ejected fluid flowing along the axial direction of the mixing section under different inlet pressures, and the change of the mass transfer rate between it and the auxiliary working fluid, respectively. Four pressure conditions were considered, with a pressure difference of 0.01 bar between each section. As observed in the figure, when the pressure of the ejected fluid increased from 2.46 bar to 2.49 bar, the velocity of the ejected fluid in the mixing section increased from 121.63 m/s to 132.96 m/s. Increasing the initial velocity reduces the velocity difference between the auxiliary working fluid and the entrained fluid in the mixing chamber. This, in turn, decreases the mass transfer rate between the auxiliary working fluid and the ejected fluid and reduces the area of the ejected fluid due to mass transfer and erosion by the auxiliary working fluid. Consequently, an increase in the inlet pressure of the ejected fluid results in a higher volume of ejected fluid in the mixing chamber. This leads to an increase in the ejection coefficient of the mixed nozzle ejector and enhances the efficiency of the new absorption suction ejector cold power combined supply cycle.

As shown in Fig. 10 (d) and (e), the temperature of the ejected fluid and the condensing mass transfer rate between the ejected fluid and the auxiliary working fluid decrease with the increasing pressure. The reason for this is that the velocity difference between the ejected fluid and the auxiliary fluid decreases, resulting in a decrease in the energy transfer between the auxiliary fluid and the ejected fluid, and the temperature rise of the ejected fluid slows down. Therefore, increasing the pressure of the ejected fluid will also cause the mixing speed between the ejected fluid and the auxiliary working fluid to slow down, and the temperature difference between them to increase. As a result, the temperature rise of the ejected fluid at the low pressure inlet is higher than that at the high pressure inlet at the mixing chamber outlet.

Fig. 10(f) illustrates the impact of the ejected fluid on the ejection coefficient under varying pressures and saturations. In this context, saturation is defined as the ratio of saturation pressure to the actual pressure at equilibrium. It is evident from the figure that as the ejector pressure increases, the ejection coefficient of the hybrid nozzle ejector also increases. In the test range of this paper, the increase of pressure difference by 9 kPa leads to an increase of about 30 % in the ejection coefficient. The reason for this phenomenon is that, when the inlet saturation of the ejected fluid and the nozzle outlet pressure are fixed, a higher inlet pressure of the ejected fluid results in a larger pressure differential between the ejected fluid inlet and the working nozzle outlet. The ejected fluid is more readily propelled into the premix chamber by the pressure, resulting in an increase in velocity within the

Table 5
Performance of the individual components and the overall system.

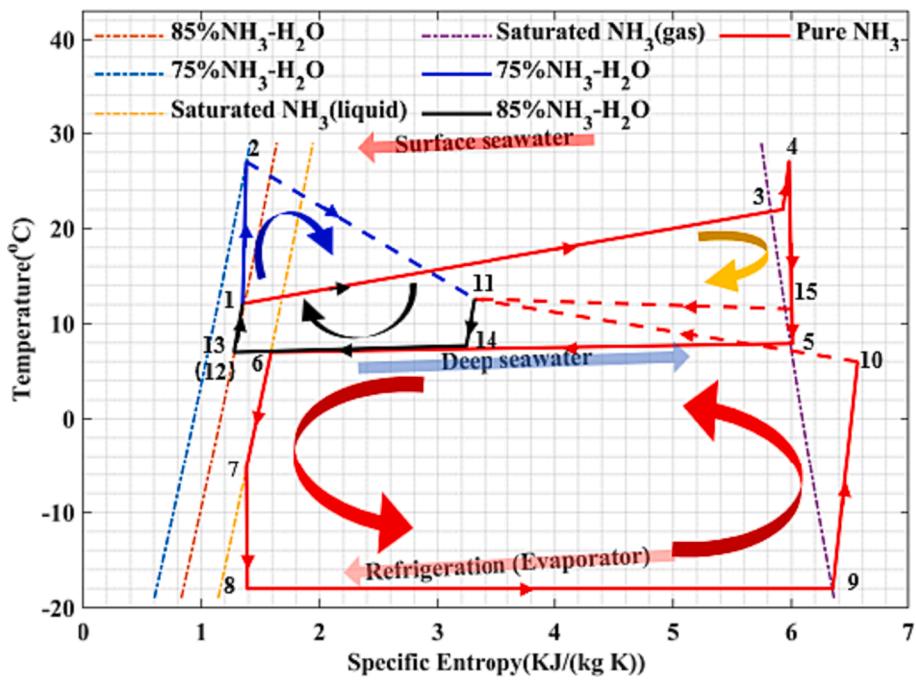| Component	Value	Component	Value
$\dot{Q}_G$(kW/kg)	1381.02	$\dot{W}_P$(kW/kg)	3.48
$\dot{Q}_R$(kW/kg)	14.11	$\dot{W}_T$(kW/kg)	25.51
$\dot{Q}_A$(kW/kg)	1373.44	η_{power}	1.58 %
$\dot{Q}_E$(kW/kg)	243.47	η_{ref}	17.45 %
$\dot{Q}_C$(kW/kg)	238.63		

Fig. 6. Temperature-Specific entropy diagram of the OTEC cycle.

premix chamber and providing greater kinetic energy at the entrance of the mixing chamber. Furthermore, as observed from the figure, when the inlet pressure of the ejecting fluid remains constant, varying the saturation of the ejecting fluid has minimal impact on the ejecting co-efficient. Given that the ejected fluid is propelled by the pressure differential between the working nozzle outlet and the ejected fluid inlet, altering the saturation of the ejected fluid has little impact on the ejector ejection coefficient. Additionally, the elevated saturation leads to a lower fluid density and a larger volume of fluid that needs to be ejected. This condition is not favorable for the working fluid and auxiliary working fluid to propel the ejected fluid, resulting in a slight decrease in the ejection coefficient.

4.3. Performance analysis of the cycle under various operation conditions

The performance evaluation of the proposed OTEC cycle is influenced by various factors, including heat source temperature, cold source temperature, refrigeration temperature, initial ammonia concentration, and reflux ratio. As the temperature of the deep seawater, which serves as the cold source, experiences minimal fluctuations, this section primarily focuses on analyzing and discussing the refrigeration and power performance within the typical operating range of the cycle, including the heat source temperature, cooling temperature, initial ammonia concentration, and reflux ratio.

Fig. 11 depicts the refrigeration-power performance of the OTEC cycle at different refrigeration temperatures with varying reflux ratios. At this time, the hot/cold source temperature (30 °C and 4 °C, respectively) and ammonia concentration (85 % at point 1) remain unchanged. Absorption refrigeration cycles typically employ lithium bromide as the working medium when the refrigeration temperature is above 0 °C [28]. However, in marine fisheries and ocean energy applications for refrigeration purposes (such as seawater freezing desalination), a refrigeration temperature of approximately −18 °C is commonly needed [29]. Consequently, this paper primarily focuses on the refrigeration temperature range of approximately −18 °C. It can be seen from Fig. 11 as the refrigeration temperature increases, both the refrigeration coefficient and power coefficient of the cycle will also increase. Taking the reflux ratio of 1.5 as an example, the refrigeration coefficient increased from 17.45 % to 36.59 %, and the power coefficient increased from 1.58

% to 1.68 %. The reason for this phenomenon is that when the evaporation temperature increases, the pressure at the inlet of the ejector (point 10) also increases. This increase in pressure leads to an increase in the ejector coefficient, which in turn enhances the performance of the ejector. As a result, more ammonia mass flows into the evaporator, leading to an increase in the amount of refrigeration provided by the system. Consequently, the evaporator power per unit mass also increases, contributing to an overall improvement in the system's efficiency and performance. Additionally, as the ammonia steam required by the ejector is reduced, more ammonia steam can be used to complete the expansion work in the turbine, resulting in an increase external power output capacity of the system. This increase in turbine power, combined with the constant temperatures maintained in the generator and superheater, contributes to an overall increase in both the power coefficient and refrigeration coefficient of the system.

Additionally, the figure illustrates that the reflux ratio influences the cycle performance. Taking the refrigeration temperature of −18 °C as an example, with the increase of reflux ratio, the refrigeration coefficient decreased from 17.45 % to 10.25 %, and the power coefficient decreased from 1.58 % to 1.25 %. Within the range of reflux ratios considered in this study, elevating the reflux ratio results in higher pressures at Point 2 and Point 15. The outlet pressure of the ejector is affected by concentrated ammonia water, while the inlet pressure of the primary fluid is affected by dilute ammonia water. The pressure difference between the two decreases as the reflux ratio increases. With the same ejector size, this decrease in pressure difference is not favorable for improving the ejector performance. Consequently, the increase of the reflux ratio reduced the refrigeration and power coefficient in this cycle.

Fig. 12 shows the refrigeration-power performance of the OTEC cycle at different refrigeration temperatures with varying ammonia mass fractions. The figure demonstrates that ammonia concentration significantly impacts the refrigeration coefficient and power coefficient. With increasing concentration, the system exhibits an improvement in the power coefficient but a decrease in the refrigeration coefficient. Taking the refrigeration temperature of −18 °C as an example, in the range of 0.8–0.9 ammonia concentration, the power coefficient increases from 0.67 % to 2.01 %, but the refrigeration coefficient drops sharply from 23.53 % to 3.07 %. The influence of ammonia concentration on the system is primarily seen in two aspects. Firstly, as the ammonia mass
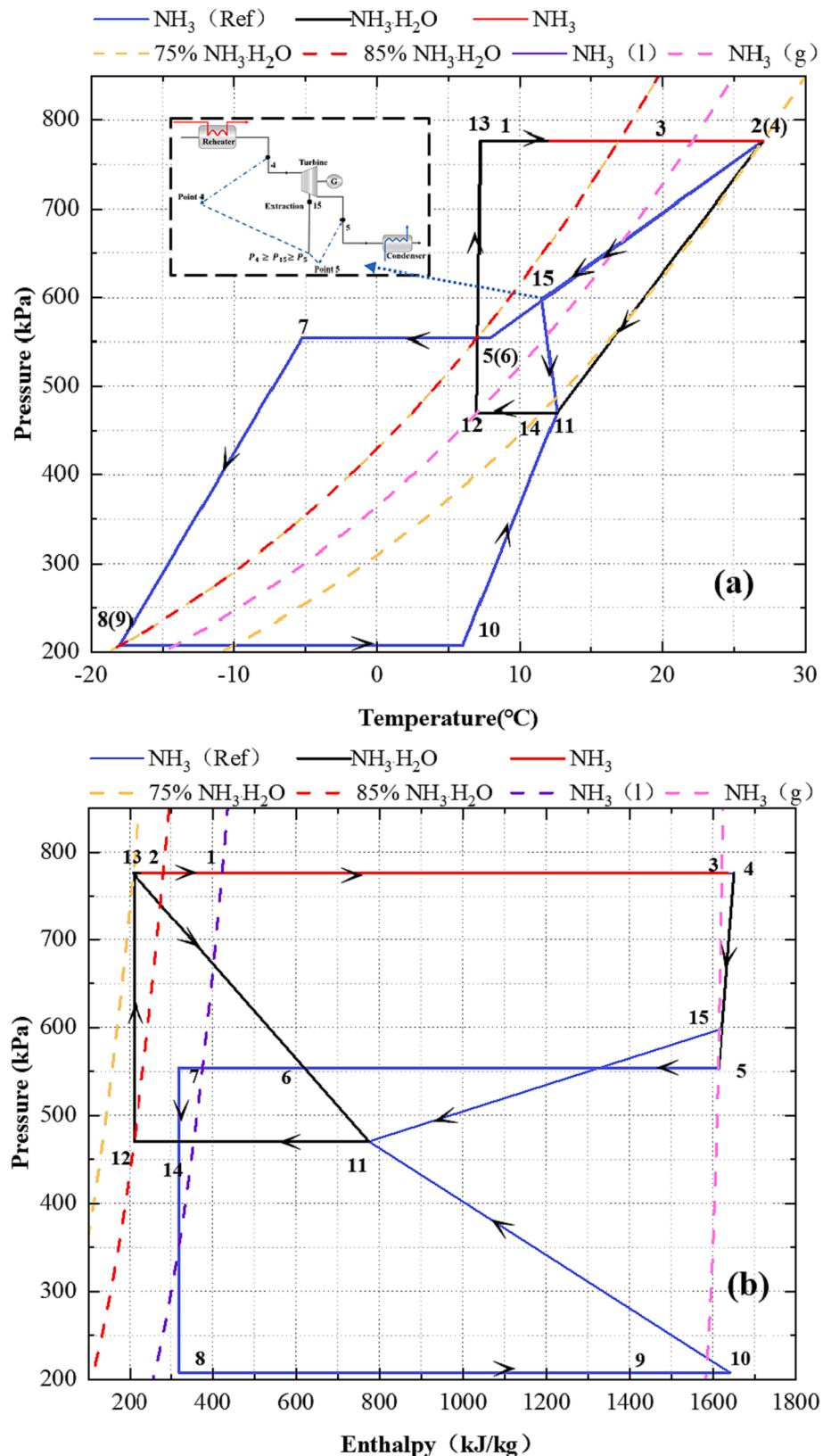
Fig. 7. State parameter diagrams of the OTEC cycle (a) Temperature-pressure; (b)Pressure-enthalpy.

concentration rises, an increase in pressure at both point 2 and point 15 leads to a corresponding elevation in the outlet pressure within the ejector nozzle. This engenders a reduction in the absolute pressure (negative pressure) at the nozzle outlet, subsequently weakening the suction effect at point 10. Consequently, the efficient entrainment of both the mainstream and auxiliary fluids decreases with the same ejector size, leading to a reduction in the refrigeration flow rate and refrigeration coefficient. Secondly, an increase in initial concentration

Fig. 8. Exergy loss analysis of the present OTEC system.

Fig. 9. Pressure distribution of three fluids in the ejector.

results in higher pressure, which positively impacts the system's power output capacity. Within an appropriate range, a higher initial concentration leads to a decrease in generator power while improving the power coefficient of the system.
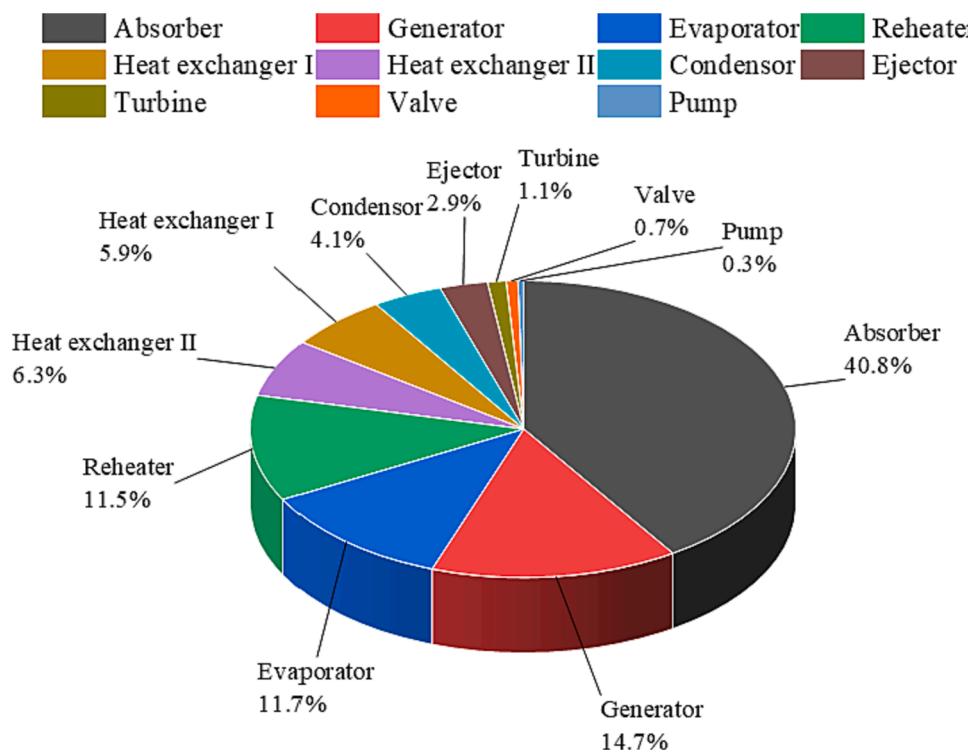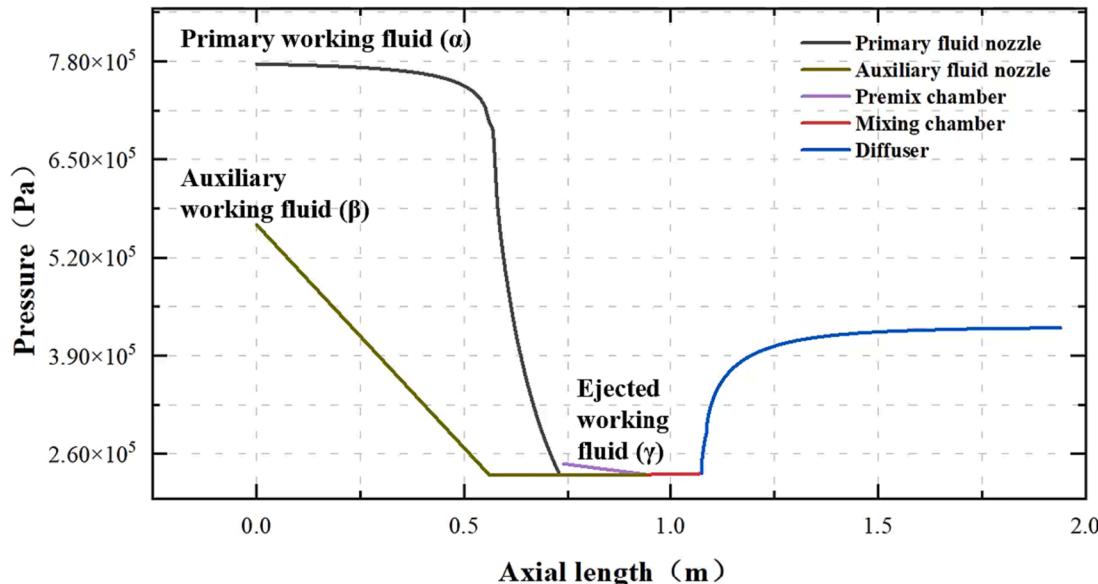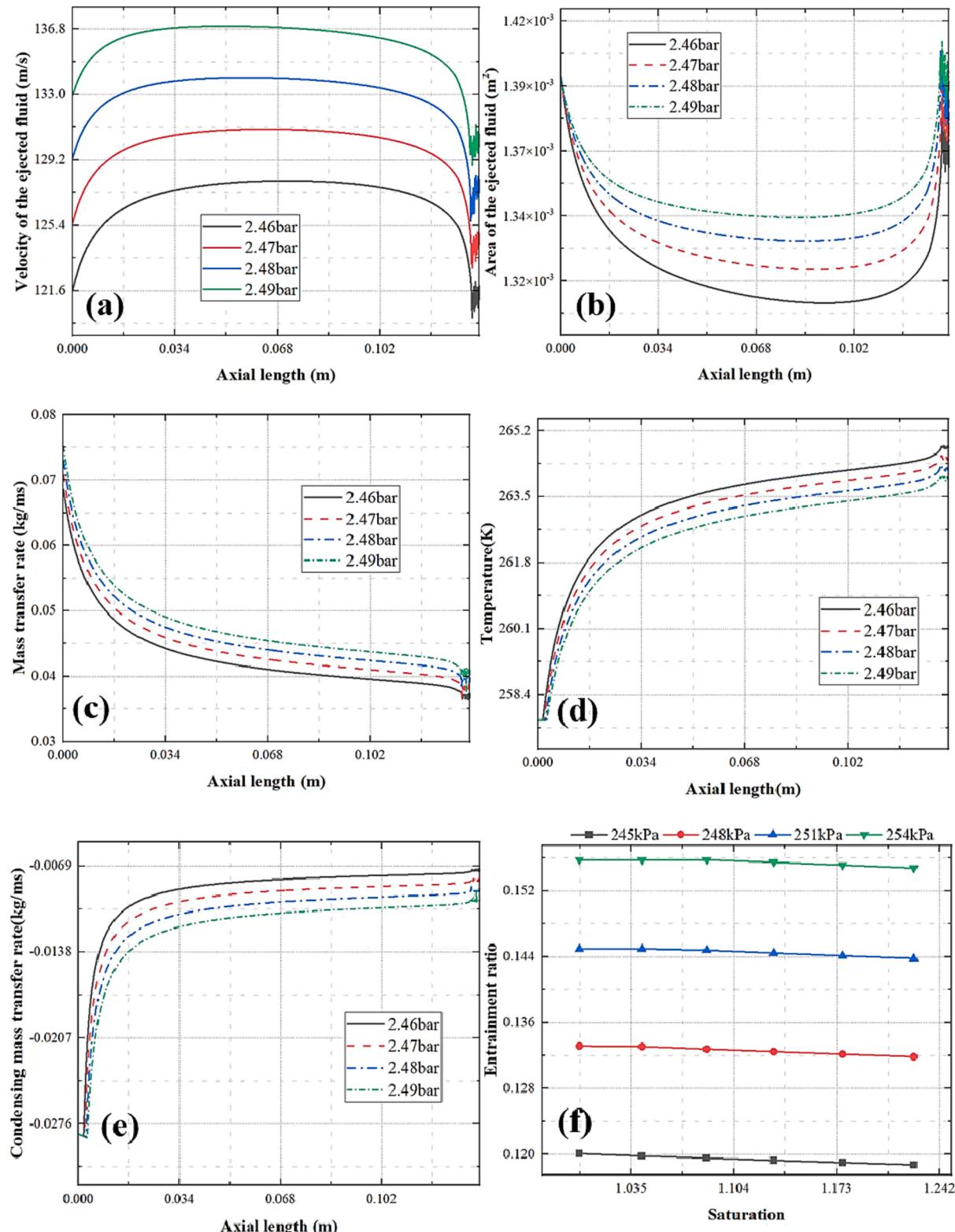
Fig. 13 represents the refrigeration-power performance of the OTEC cycle at different heat source temperatures with varying reflux ratios. At this time, the refrigeration temperature (-18 °C), cold source temperature (4 °C), and ammonia concentration (85 % at point 1) remain constant. It is observed that as the heat source temperature increases, the refrigeration coefficient decreases while the power coefficient increases. Taking the reflux ratio = 1.5 as an example, in the range of heat source

temperature 27–32 °C, the refrigeration coefficient decreased from 22 % to 13 %, and the power coefficient increased from 1.16 % to 1.78 %. This situation occurs because, with a fixed heat transfer temperature of the generator, an increase in the heat source temperature results in the generator absorbing more heat, improving its efficiency. Since the condensation temperature remains unchanged, the high-temperature pure ammonia can generate more work in the turbine, leading to an increase in turbine power and the system's power coefficient. With an increase in the temperature of the heat source, the pressure and temperature of the dilute ammonia water at the outlet of the rectifier (point 2) also increase. Thus, the outlet pressure of the working nozzle

Fig. 10. Parameter variation of the ejected fluid under different pressure inlet (a: velocity of the ejected fluid; b: area of the ejected fluid; c: mass transfer rate; d: temperature; e: condensing mass transfer rate; f: entrainment ratio).

increases, while the gas holding rate and ejection coefficient decrease. Simultaneously, as the refrigeration temperature remains unchanged and the power of the generator increases, the refrigeration coefficient of the system decreases with the rise in heat source temperature.

The non-working region in Fig. 13 refers to the region where the ejector cannot operate. The main reason is that as the heat source

temperature increases, the inlet pressure of both the main flow and the auxiliary flow also increases. With the same ejector size, if the outlet pressure exceeds the pressure of the ejected fluid (point 10), the ejector cannot function properly. This emphasizes the importance of accurately calculating the ejector size based on the specific field conditions in practical engineering.
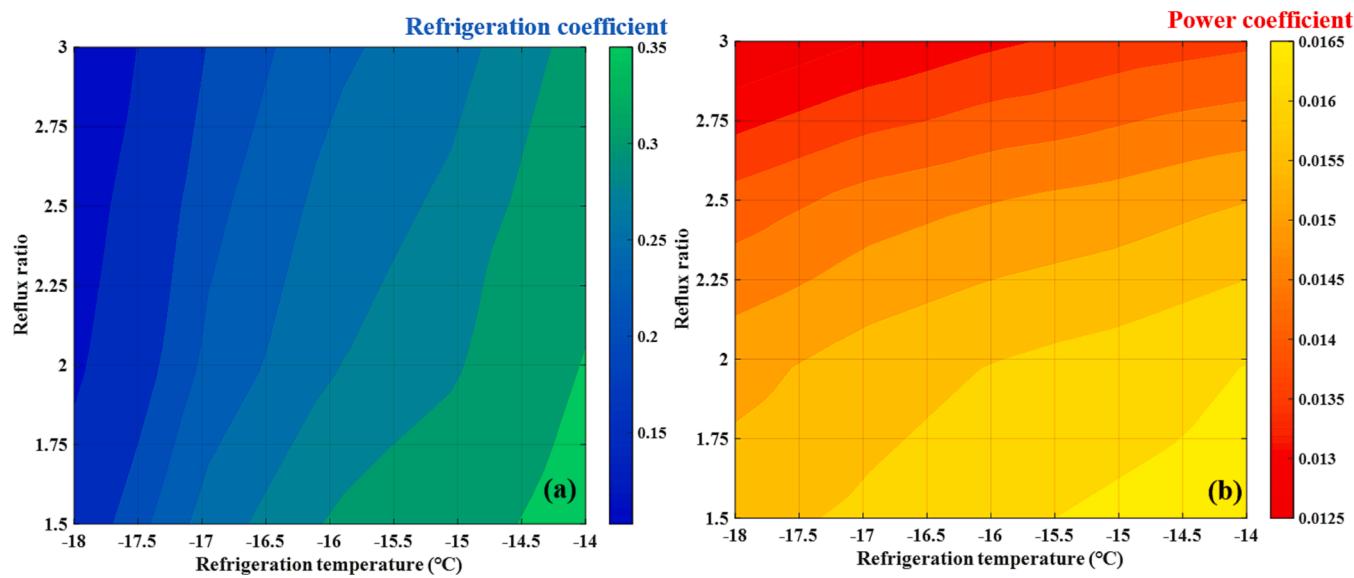
Fig. 11. Refrigeration-power performance of the OTEC cycle at different refrigeration temperatures with varying reflux ratios.
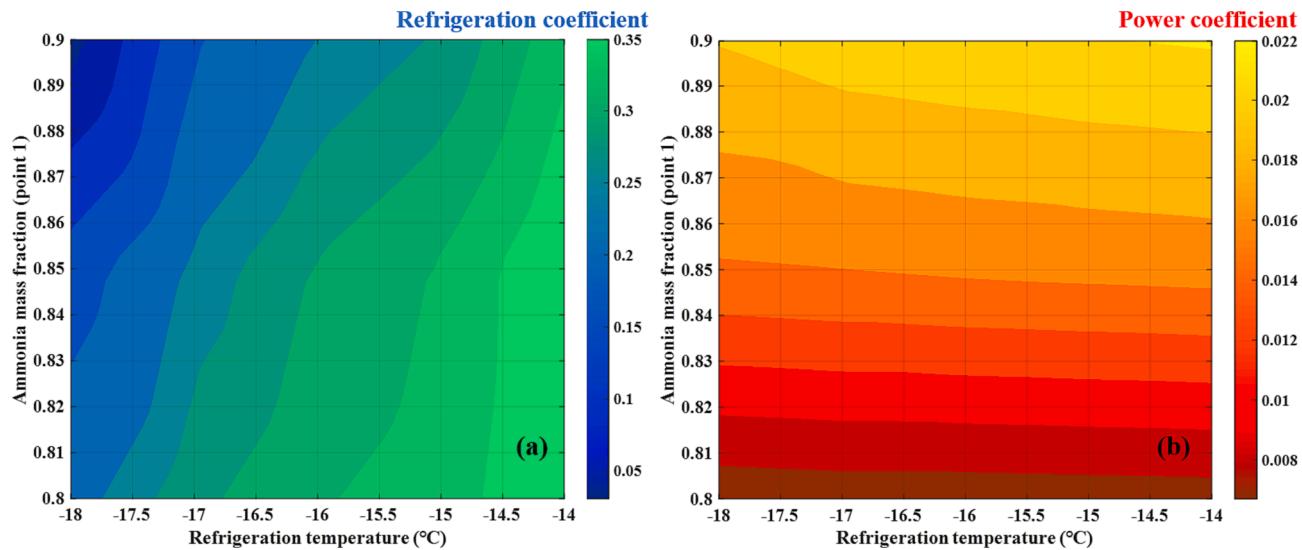

Fig. 12. Refrigeration-power performance of the OTEC cycle at different refrigeration temperatures with varying ammonia mass fractions.

Fig. 14 shows the refrigeration-power performance of the OTEC cycle at different heat source temperatures with varying ammonia mass fractions. When the refrigeration temperature and reflux ratio (=1.5) are held constant, the refrigeration coefficient decreases with an increase in concentration. Similar to the reasons mentioned earlier, this is primarily attributed to the reduced entrainment of both the mainstream and auxiliary fluids with increasing concentration. Additionally, the power coefficient increases. This is due to the rise in concentration while keeping the reflux ratio constant. If the cycle operates normally, the power of cycle absorption units, such as the generator, decreases, resulting in a lower denominator for the power coefficient. This change contributes to the improvement of the power coefficient. However, if the cold source temperature entering the absorber and the heat transfer temperature difference within the absorber are known, the pressure drop in the absorber is influenced by the concentration of ammonia water and the gas content of ammonia water. A higher concentration of ammonia solution corresponds to a greater gas content, resulting in higher pressure within the absorber. Conversely, a lower concentration leads to a lower gas content and subsequently lower pressure. The

concentration of concentrated ammonia exhibits a positive correlation with the system power coefficient. A higher concentration of concentrated ammonia results in a greater system power coefficient. However, this can make absorption in the absorber more challenging and significantly impact the absorber pressure.

4.4. Performance comparison with different low temperature difference cycles

It's important to emphasize that, for highlighting the benefits of employing liquid–gas-gas ejectors to enhance OTEC performance, the performance comparison is segmented into two aspects: first, a comparison with the OTEC cycle using the conventional liquid–gas ejector; and second, a comparison with previously published low-temperature differential thermal cycle research.

The conventional liquid–gas ejector employs direct high-pressure diluted ammonia water as the mainstream fluid for ejecting working fluid. Under the same size as the ejector discussed in this paper, the OTEC cycles of both the single nozzle (liquid–gas) ejector and the hybrid
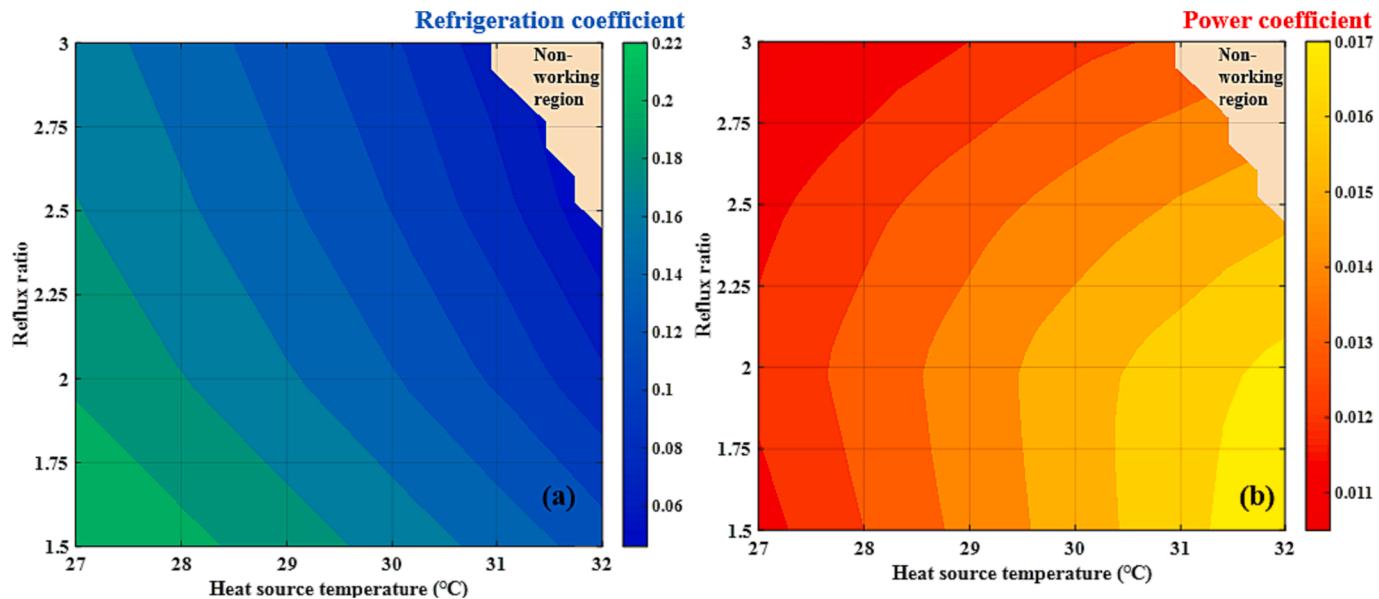
Fig. 13. Refrigeration-power performance of the OTEC cycle at different heat source temperatures with varying reflux ratios.
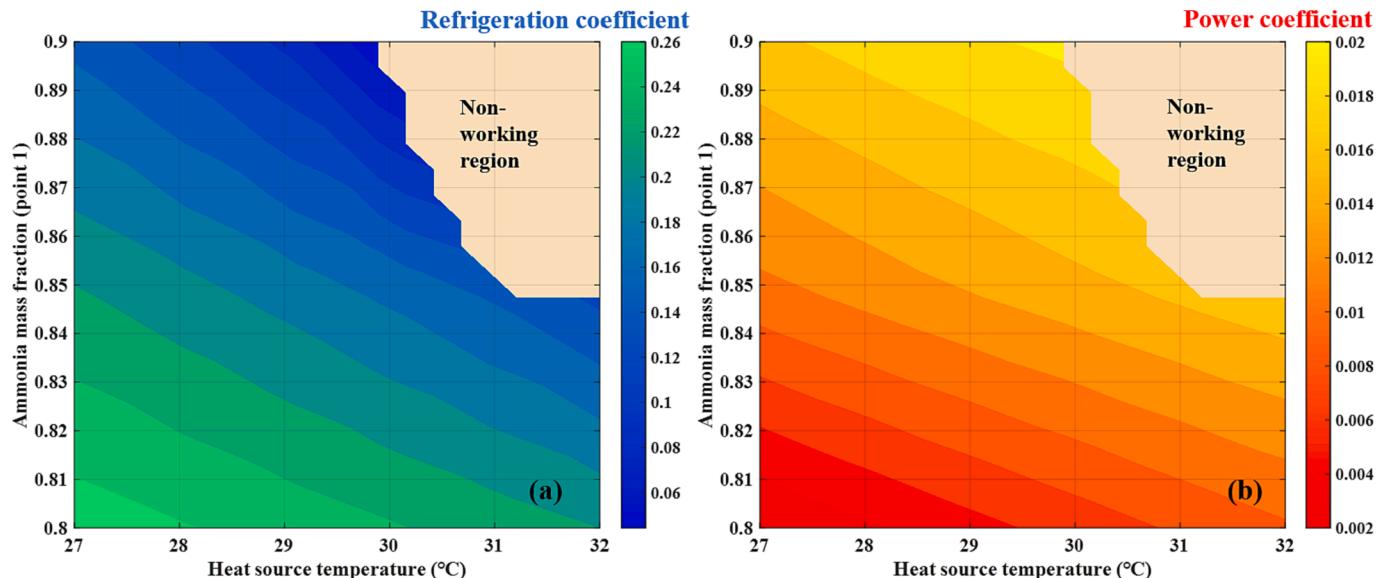

Fig. 14. Refrigeration-power performance of the OTEC cycle at different heat source temperatures with varying ammonia mass fractions.

nozzle (liquid–gas-gas) ejector under varying refrigeration temperatures are illustrated in Fig. 15. As evident from the graph, the OTEC cycle utilizing the liquid–gas-gas ejector attains a lower cooling temperature of −18.8 °C, whereas the OTEC cycle involving the liquid–gas ejector reaches a minimum cooling temperature of −15.6 °C. The results indicate that the proposed cycle reduces the minimum cooling temperature by 20.5 % compared to the cycle utilizing the liquid–gas ejector. At the same refrigeration temperature of −15 °C, the power coefficient of the OTEC cycle utilizing the liquid–gas-gas ejector exhibits a slight increment (2.47 %) when compared with the traditional ejector, yet there is a substantial enhancement (114.92 %) in the refrigeration coefficient. This observation underscores that the novel OTEC cycle utilizing the liquid–gas-gas ejector yields significant enhancements in refrigeration-power co-supply performance compared to the OTEC cycle using the liquid–gas ejector.

Various studies have utilized diverse methods for evaluating the cycle. In this study, to facilitate comparison and analysis, both

refrigeration and power output are converted into work output. The following methods are employed for calculation.

For power output W_{power}:

$$W_{power} = \sum W_{out} - \sum W_{in} \tag{41}$$

So the power efficient is:

$$\eta_{Power} = \frac{W_{power}}{\sum Q_{in}} \tag{42}$$

The refrigeration coefficient is:

$$\eta_{ref} = \frac{Q_{Ref}}{\sum Q_{in}} \tag{43}$$

Table 6 displays the comparisons among various cycle types in the low-temperature difference context. While this cycle may not possess the same work capacity as cycles exclusively designed for work, as seen in Refs. [27,31,32], etc., the current cycle demonstrates notable
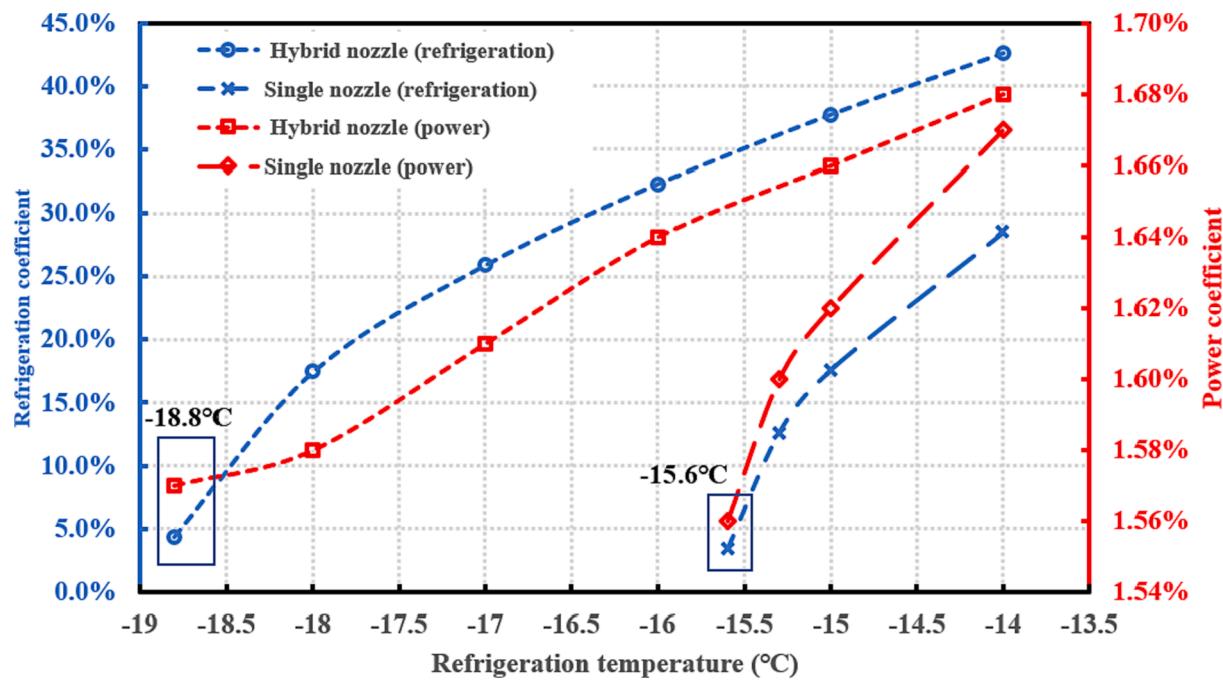
Fig. 15. Performance comparison of the OTEC cycle using hybrid and single nozzle.

Table 6
Performance comparison between the present cycle and other cycles.

Cycle type	Working fluid	Heat temperature ∘C	Cold temperature ∘C	Refrigeration temperature ∘C	Power coefficient	Refrigeration coefficient
Absorption [9]	NH_3–H_2O	30	5	/	0.3–0.8 %	/
Absorption [27]	NH_3–H_2O	28	4	/	2.94 %	/
Rankine[30]	R134a	27	4.5–5	/	0.8–1.1 %	/
Rankine[31]	R22	26	5	/	1.90 %	/
Rankine[32]	R1234yf	30	4	/	2.57 %	/
Combined cycle[8]	NH_3–H_2O R600a	133	35	−8	10.28 %	15.54 %
Combined cycle[33]	NH_3 H_2O	26	4.5	14	1.23 %	6.27 %
Ejection[34]	R123	150	25	−10	6–7 %	4–15 %
Ejection[35]	R601	120	4.5	10	5.25 %	9.02 %
Ejection[36]	R245fa	150	30	5	8.27 %	1.65 %
The present work	NH_3–H_2O	30	4	−18	1.58 %	17.45 %

enhancements when considering its integration into the cold-power combined cycle, as indicated in reference [33]. It's worth noting that the refrigeration capacity of this cycle significantly exceeds that of cycles operating at higher temperature differences, as demonstrated in Refs. [34–36]. Notably, the temperature difference for this cycle is only 26 °C. A comparative analysis reveals that the novel OTEC cycle employing liquid–gas-gas ejectors, while preserving its work capacity, exhibits distinct advantages in refrigeration performance.

The primary factor contributing to the performance enhancement is the effective utilization of auxiliary ammonia vapor. By harnessing the pressure energy of dilute ammonia water and the kinetic energy from turbine pumping, the combined operation of two nozzles results in fluid ejection. Additionally, the introduction of an auxiliary fluid establishes a beneficial pressure differential during the ejection process. This pressure reduction ensures efficient entrainment and entrapment of the ejected fluid by the mainstream fluid, thereby facilitating the desired flow and mixing patterns. In summary, the cycle can effectively enhance both power and refrigeration output to a certain extent.

5. Conclusions

This paper proposed a novel combined power-refrigeration cycle based on a liquid–gas-gas ejector to enhance the efficiency of OTEC. Additionally, a hybrid nozzle ejector model that considered the phase transformation and mass transfer process of binary working medium was established. Building upon the thermodynamic analysis and performance comparison of the novel OTEC cycle, the main conclusions are listed as follows:

1. The incorporation of auxiliary fluids in the ejector enhances the pressure differential favorably for the ejection process. In the test range of this paper, the increase of pressure difference by 9 kPa leads to an increase of about 30 % in the entrainment coefficient.
2. The liquid–gas-gas ejector contributes merely 2.9 % to the overall exergy loss of the system, which demonstrates its efficacy as a kinetic energy conversion unit.
3. One of the significant factors contributing to the variation in cycle performance is the alteration in pressure difference within the ejector. Changes in heat source temperature, ammonia mass fraction, and reflux ratio can impact the pressure difference inside the ejector.

4. The proposed cycle reduces the minimum cooling temperature by 20.5 % compared to the cycle utilizing the liquid–gas ejector. At the same refrigeration temperature, the power efficiency increased by 2.47 %, and the cooling efficiency increased by 114.92 %.

5. Compared to the previous studies, the proposed cycle achieves a power/refrigeration efficiency of 1.58 %/17.45 % at a refrigeration temperature of −18 °C. Even though the temperature difference for this cycle is only 26 °C, its refrigeration capacity notably surpasses that of cycles operating at higher temperature differences

CRediT authorship contribution statement

Ji Zhang: Conceptualization, Methodology, Software, Validation, Formal analysis, Funding acquisition, Investigation, Resources, Data curation, Writing – original draft, Writing – review & editing. **Zhixiang Zhang:** Data curation, Methodology, Software, Formal analysis. **Shiqiao Zhou:** Data curation, Investigation. **Hongxun Hui:** Writing – review & editing. **Ning Mei:** Conceptualization, Resources. **Han Yuan:** Conceptualization, Methodology, Software, Validation, Formal analysis, Funding acquisition, Investigation, Resources, Data curation, Writing – original draft, Writing – review & editing.

Declaration of Competing Interest

The authors declare that they have no known competing financial interests or personal relationships that could have appeared to influence the work reported in this paper.

Data availability

Data will be made available on request.

Acknowledgments

Appendix A. . Parameter determination and equation solving of the ejector model

Since the parameter determination of the nozzle section and the premix chamber has been listed in the main text, this section will focus on describing the parameter determination and equation solving in the mixing chamber and diffuser chamber. The following parameters correspond to Eq. (25)-(37).

For the condensing mass transfer, $\frac{d\Gamma_c}{dl}$ represents the condensing mass transfer differential between the working fluid and the auxiliary working fluid caused by the temperature difference, and $\frac{d\Gamma'_c}{dl}$ represents the condensing mass transfer differential between the auxiliary working fluid and the ejected fluid. The expressions are as follows:

$$\frac{d\Gamma_c}{dl} = \frac{\alpha_{int}\left(T_\alpha - T_\beta\right)}{h_{int} - h_{l,sat}} \frac{dF_{int}}{dl} \tag{A.1}$$

$$\frac{d\Gamma'_c}{dl} = \frac{\alpha'_{int}\left(T_\gamma - T_\beta\right)}{h'_{int} - h_{l,sat}} \frac{dF'_{int}}{dl} \tag{A.2}$$

Where, α_{int}, α'_{int} represent the thermal diffusivity between the working fluid and the auxiliary working fluid, and between the auxiliary working fluid and the ejection fluid, respectively. F_{int}, F'_{int} represent the contact area between the working fluid and the auxiliary working fluid, and between the auxiliary working fluid and the ejection fluid, respectively.

For the desorption and absorption process of the ammonia water: when ammonia gas is absorbed in water, the chemical reaction of the process mainly occurs at the liquid film side of the phase interface, and the reaction equation is:

$$NH_3(aq) + H_2O(l) \leftrightarrow NH_3 \cdot H_2O(aq) \tag{A.3}$$

$$NH_3(aq) + H_2O(l) \leftrightarrow NH_4^+(aq) + OH^-(aq) \tag{A.4}$$

In the aqueous ammonia solution formed by the reaction of ammonia gas and water, ammonia monohydrate primarily exists in molecular form within the solution. However, as the temperature increases, ammonia monohydrate decomposes and releases ammonia gas from the solution. The process of ammonia being absorbed or desorbed from the droplet is mainly directly driven by the partial pressure of the two phases, and the mass transfer rate is:

$$\Gamma_{NH_3} = M_{NH_3} K_{NH_3} A\left(P_{NH_3,g} - P_{NH_3,d}^{eq}\right) \tag{A.5}$$

Where, Γ_{NH_3} is the mass transfer of the desorption and absorption process, M_{NH_3} is the molecular mass of ammonia gas, A is the surface area of the droplet, $P_{NH_3,g}$ is the partial pressure of ammonia gas, and $P_{NH_3,d}^{eq}$ is the equilibrium pressure corresponding to the concentration of ammonia in the droplet [37].

$$P_{NH_3,d}^{eq} = H_{NH_3}\left(1 - 3.4182r + 3.0002r^2\right)\chi_{NH_3}\exp\left(0.0333\chi_{NH_3} - 0.0123\right) \tag{A.6}$$

where, χ is the concentration of ammonia, H_{NH_3} is the Henry constant of the temperature function, the expression is as follows:

$$\ln\left(H_{NH_3}\right) = \left(-681.53\right)/T + 28.67\cdot\ln(T) + \left(-0.054\right)\cdot T + \left(-151.37\right) \tag{A.7}$$

The total mass transfer $\frac{1}{K_{NH_3}}$ resistance is determined by the combined mass transfer resistances in the gas and liquid films according to the two-film theory

$$\frac{1}{K_{NH_3}} = \frac{1}{K_{NH_3,g}} + \frac{H_{NH_3}}{EK_{NH_3,aq}} \tag{A.8}$$

where, $K_{NH_3,g}$ is the mass transfer coefficient of gas, $K_{NH_3,aq}$ is the mass transfer coefficient of liquid, E is a mass transfer enhancer that enhances gas absorption in chemical reactions. $K_{NH_3,g}$ is determined by the Ranz-Marshall model [38]:

$$\frac{K_{NH_3,g}D_dRT}{D_{NH_3}} = 2 + 0.69Re_d^{05}Sc^{0.33} \tag{A.9}$$

where, D_d is the droplet diameter, D_{NH_3} is the binary diffusion coefficient of ammonia in the gas, Re_d is the relative Reynolds number, Sc is the Schmidt number.

$K_{NH_3,aq}$ is determined by the Hsu and Shih model [39]:

$$K_{NH_3,aq} = 0.88\sqrt{fD_{NH_3,aq}} \tag{A.10}$$

$$f = \sqrt{\frac{8\sigma}{3\pi m_{aq}}} \tag{A.11}$$

where, $D_{NH_3,aq}$ is the binary diffusion coefficient of ammonia in liquid, m_{aq} is the droplet mass. The reaction between ammonia and water is the first-order reaction, so the expression is:

$$E = \frac{\sqrt{K_{app}D_{NH_3,aq}}}{k_{NH_3,aq}} \tag{A.12}$$

where, K_{app} is the reaction rate constant.

In this study, the deposition mass transfer of the working medium between the fluids is neglected, and only the mass transfer resulting from the entrainment of the working medium with low flow rate by the working medium with high flow rate is considered. Based on Kolev's theory [40], the entrainment mass transfer differential can be expressed as:

$$\frac{d\Gamma_{\alpha\to\beta}}{dl} = \begin{cases} 1.175 \times 10^{-4}m\cdot s\cdot kg^{-1} \times w_\alpha\sqrt{\rho_\alpha\rho_\beta}\,\eta_\beta\big(Re_\beta - Re_{\beta,\infty}\big)\dfrac{dF_{int}}{dl}\ (Re_\beta{\geqslant}Re_{\beta,\infty}) \\ 0\ (Re_\beta < Re_{\beta,\infty}) \end{cases} \tag{A.13}$$

$$\frac{d\Gamma_{\gamma\to\beta}}{dl} = \begin{cases} 1.175 \times 10^{-4}m\cdot s\cdot kg^{-1} \times w_\gamma\sqrt{\rho_\gamma\rho_\beta}\,\eta_\beta\big(Re_\beta - Re'_{\beta,\infty}\big)\dfrac{dF'_{int}}{dl}\ (Re_\beta{\geqslant}Re'_{\beta,\infty}) \\ 0\ (Re_\beta < Re'_{\beta,\infty}) \end{cases} \tag{A.14}$$

where, $\frac{d\Gamma_{\alpha\to\beta}}{dl}$ represents the mass transfer resulting from the working fluid being entrained by the auxiliary working fluid, while $\frac{d\Gamma_{\gamma\to\beta}}{dl}$ represents the mass transfer resulting from the ejected fluid being entrained by the auxiliary working fluid. $Re_{\beta,\infty}$ and $Re'_{\beta,\infty}$ are locally equilibrium membrane Reynolds numbers:

$$Re_{\beta,\infty} = \exp\left(5.8504 + 0.4249\frac{\eta_\alpha}{\eta_\beta}\sqrt{\frac{\rho_\beta}{\rho_\alpha}}\right) \tag{A.15}$$

$$Re'_{\beta,\infty} = \exp\left(5.8504 + 0.4249\frac{\eta_\gamma}{\eta_\beta}\sqrt{\frac{\rho_\beta}{\rho_\gamma}}\right) \tag{A.16}$$

where, η_α, η_β, η_γ represent the dynamic viscosity of the working fluid, the auxiliary working fluid, and the ejected fluid, respectively.

$\frac{d\Pi}{dL}$ and $\frac{d\Pi'}{dl}$ represent the momentum transfer differential at the interface between the working fluid and the auxiliary working fluid, and the momentum transfer differential at the interface between the auxiliary working fluid and the ejected fluid, respectively.

$$\frac{d\Pi}{dl} = \frac{1}{2}\rho_\beta C_{\alpha-\beta}|w_\alpha - w_\beta|(w_\beta - w_\alpha)\frac{dF_{int}}{dl} \tag{A.17}$$

$$\frac{d\Pi'}{dl} = \frac{1}{2}\rho_\beta C_{\gamma-\beta}|w_\gamma - w_\beta|(w_\beta - w_\gamma)\frac{dF'_{int}}{dl} \tag{A.18}$$

Where, C is the interfacial resistance coefficient between fluids

$$C_{\alpha-\beta} = a_1Re_{\alpha-\beta}^{-0.25} \tag{A.19}$$

$$C_{\gamma-\beta} = a_2Re_{\gamma-\beta}^{-0.25} \tag{A.20}$$

$$Re_{\alpha-\beta} = \frac{1}{\mu_\beta}(w_\alpha - w_\gamma)D_1\sqrt{\frac{A_\beta}{A_\alpha + A_\beta}} \tag{A.21}$$

$$Re_{\gamma-\beta} = \frac{1}{\mu_\beta}(w_\beta - w_\gamma)D_2\sqrt{\frac{A_\beta}{A_\gamma + A_\beta}} \tag{A.22}$$

where, a_1, a_2 are constant, μ is the kinematic viscosity.

$\frac{dZ_{f,int}}{dl}$, $\frac{dZ'_{f,int}}{dl}$ and $\frac{dZ_{f,w}}{dl}$ represent the differential frictional forces between the working fluid and auxiliary working fluid, auxiliary working fluid and ejection fluid, and ejection fluid and wall surface, respectively. The calculation formulas are as follows:

$$\frac{dZ_{f,int}}{dl} = 0.5f_{int}\rho_a\left(w_\beta - w_\alpha\right)^2\frac{dF_{int}}{dl} \tag{A.23}$$

$$\frac{dZ'_{f,int}}{dl} = 0.5f'_{int}\rho_a\left(w_\beta - w_\gamma\right)^2\frac{dF'_{int}}{dl} \tag{A.24}$$

$$\frac{dZ_{f,w}}{dl} = 0.5f_w\rho_\beta w_\gamma^2\frac{dF_w}{dl} \tag{A.25}$$

Where, f is the friction factor, determined by the Churchill model [41].

The parameters on the interface of the two-phase flow w_{int}, h_{int} are determined according to the condensation direction at the interface.

When $T_\alpha > T_\beta$,

$$w_{int} = w_\alpha, h_{int} = h_\alpha \tag{A.26}$$

When $T_\gamma > T_\beta$

$$w_{int} = w_\gamma, h_{int} = h_\gamma \tag{A.27}$$

Appendix B. . Determination of ejector structure and geometric conditions

1. Nozzle segment

The local sound velocity at the primary fluid nozzle section is calculated using the two-phase flow calculation formula, and it corresponds to the throat velocity.

$$a_* = a_M \tag{B.1}$$

The inlet parameters of the mixed nozzle ejector for the primary fluid nozzles can be obtained based on the proposed cycle in this paper. The partial differential equations of the nozzle section are then solved using the known inlet parameters as the initial parameters for the nozzle control equation. The equation is solved to determine the flow velocity of the fluid in the flow path. At this critical state, the cross-sectional area of the nozzle throat can be obtained by applying the mass conservation equation.

$$A_* = m_z/(\rho_* w_*) \tag{B.2}$$

Here, the subscript * denotes the throat point of the nozzle. The length of the nozzle is determined by the tilt angle of the nozzle wall. A larger tilt angle results in a shorter nozzle length and reduces fluid friction loss along the path. Conversely, a smaller tilt angle increases the nozzle length and leads to higher fluid friction loss.

In the case of auxiliary working nozzles, where the working fluid is ammonia and ammonia is a single working medium, the local sound velocity of ammonia can be obtained from the REFPROP database. Since the local sound velocity of a single-working fluid is significantly higher than that of a two-phase flow fluid, using a diverging nozzle is adequate to fulfill the working requirements of the auxiliary working fluid section.

2. Premix chamber

When the ejection coefficient is less than 0.5, the premix chamber length is calculated by the formula:

$$l = \left[\sqrt{0.083 + 0.76u} - 0.29\right]\frac{d_1}{2a_e} \tag{B.3}$$

When the ejection coefficient is greater than 0.5,:

$$l = \frac{0.37 + u}{4.4a_e}d_1 \tag{B.4}$$

where, d_1 is the diameter of nozzle outlet for auxiliary working fluid ; a_e is an empirical coefficient. For compressible fluids, the general value ranges from 0.07 to 0.09. u is the ejection coefficient of the ejector.

3. Mixing chamber

Based on the isobaric mixing theory, when the fluid flows from the premix chamber to the mixing chamber, the working fluid, auxiliary working fluid, and ejected fluid are at the same pressure. When the ejection coefficient is less than 0.5, the mixing chamber diameter d_3 is calculated as follows:

$$d_3 = 3.4d_1\sqrt{0.083 + 0.76u} \tag{B.5}$$

When the ejection coefficient is greater than 0.5:

$$d_3 = 1.55d_1(1 + u) \tag{B.6}$$

Based on experimental data, the mixing chamber length l_2 of the ejector is typically 6–10 times the diameter of the mixing chamber.

$$l_2 = (6 - 10)d_3 \tag{B.7}$$

4. Diffuser chamber

The diffuser is typically designed with a wall tilt angle of 6-10°, and the calculation formula for the outlet cross-sectional area of the diffuser is:

$$A = \frac{m_{\alpha\beta}(1+u)}{2w_{mix}\rho_{mix}} \tag{B.8}$$

where, $m_{\alpha\beta}$ is the mixing quality of the primary working fluid and auxiliary working fluid, ρ_{mix} is the density of the mixed fluid at the outlet section of the diffuser chamber, w_{mix} is the flow rate of the mixed fluid at the outlet section of the diffuser chamber.

References

[1] Li Z, Siddiqi A, Anadon LD, Narayanamurti V. Towards sustainability in water-energy nexus: Ocean energy for seawater desalination. Renew Sustain Energy Rev 2018;82:3833–47.

[2] Zhang W, Li Y, Wu X, Guo S. Review of the applied mechanical problems in ocean thermal energy conversion. Renew Sustain Energy Rev 2018;93:231–44.

[3] Wang M, Jing R, Zhang H, Meng C, Li N, Zhao Y. An innovative Organic Rankine Cycle (ORC) based Ocean Thermal Energy Conversion (OTEC) system with performance simulation and multi-objective optimization. Appl Therm Eng 2018; 145:743–54.

[4] Rahbar K, Mahmoud S, Al-Dadah RK, Moazami N, Mirhadizadeh SA. Review of organic Rankine cycle for small-scale applications. Energ Conver Manage 2017; 134:135–55.

[5] Kalina AI. Combined-cycle system with novel bottoming cycle, (1984).

[6] Uehara H, Ikegami Y. Optimization of a closed-cycle OTEC system, (1990).

[7] Yi S, Zhang Z, Peng W, Zhang J, Yuan H. Pre-expansion ejector absorption power cycle for ocean thermal energy conversion. Energ Conver Manage 2022;269: 116151.

[8] Bian Y, Pan J, Liu Y, Zhang F, Yang Y, Arima H. Performance analysis of a combined power and refrigeration cycle. Energ Conver Manage 2019;185:259–70.

[9] Yuan H, Mei N, Hu S, Wang L, Yang S. Experimental investigation on an ammonia-water based ocean thermal energy conversion system. Appl Therm Eng 2013;61: 327–33.

[10] Yoon J-I, Son C-H, Seol S-H, Kim H-U, Ha S-J, Jung S-H, et al. Performance analysis of OTEC power cycle with a liquid–vapor ejector using R32/R152a. Heat Mass Transf 2015;51:1597–605.

[11] Xue H, Liu Y, Hou Y, Xu X, Chen Y, Liu W. Study and development of closed-cycle systems of ocean thermal energy conversion. J Ocean Technol 2018;37:109–21.

[12] Hu Z, Fan C, Gao W, Chen Y. Experimental study of a miniature organic Rankine cycle unit using ocean thermal energy. Energ Conver Manage 2023;293:117494.

[13] Zhou S, Liu X, Zhang K, Yue Q, Bian Y, Shen S. Evaluation of a novel ammonia-water based combined cooling, desalination and power system based on thermodynamic and exergoeconomic analyses. Energ Conver Manage 2021;239: 114176.

[14] Geng D, Gao X. Thermodynamic and exergoeconomic optimization of a novel cooling, desalination and power multigeneration system based on ocean thermal energy. Renew Energy 2023;202:17–39.

[15] Yuan H, Mei N, Zhou P. Performance analysis of an absorption power cycle for ocean thermal energy conversion. Energ Conver Manage 2014;87:199–207.

[16] Yuan H, Zhou P, Mei N. Performance analysis of a solar-assisted OTEC cycle for power generation and fishery cold storage refrigeration. Appl Therm Eng 2015;90: 809–19.

[17] Zhang Z, Yuan H, Mei N. Theoretical analysis on extraction-ejection combined power and refrigeration cycle for ocean thermal energy conversion. Energy 2023; 273:127216.

[18] Baek S, Ko S, Song S, Ryu S. Numerical study of high-speed two-phase ejector performance with R134a refrigerant. Int J Heat Mass Transf 2018;126:1071–82.

[19] Li Y, Deng J, Ma L. Experimental study on the primary flow expansion characteristics in transcritical CO2 two-phase ejectors with different primary nozzle diverging angles. Energy 2019;186:115839.

[20] Lear W, Parker G, Sherif S. Analysis of two-phase ejectors with Fabri choking. Proc Inst Mech Eng C J Mech Eng Sci 2002;216:607–21.

[21] Banasiak K, Hafner A. 1D Computational model of a two-phase R744 ejector for expansion work recovery. Int J Therm Sci 2011;50:2235–47.

[22] Attou A, Seynhaeve J-M. Steady-state critical two-phase flashing flow with possible multiple choking phenomenon: Part 1: physical modelling and numerical procedure. J Loss Prev Process Ind 1999;12:335–45.

[23] Ameur K, Aidoun Z, Ouzzane M. Modeling and numerical approach for the design and operation of two-phase ejectors. Appl Therm Eng 2016;109:809–18.

[24] Němec T. Homogeneous bubble nucleation in binary systems of liquid solvent and dissolved gas. Chem Phys Lett 2016;467:26–37.

[25] He J, Liu J, Xu X. Experimental investigation of single bubble growth in the boiling of the superheated liquid mixed refrigerants. Int J Heat Mass Transf 2018;127: 553–65.

[26] Narabayashi T, Mizumachi W, Mori M. Study on two-phase flow dynamics in steam injectors. Nucl Eng Des 1997;175:147–56.

[27] Yuan H, Mei N, Li Y, Yang S, Hu S, Han Y. Theoretical and experimental investigation on a liquid-gas ejector power cycle using ammonia-water. Sci China-Technol Sci 2013;56:2289–98.

[28] Karakas A, Egrican N, Uygur S. Second-law analysis of solar absorption-cooling cycles using lithium bromide/water and ammonia/water as working fluids. Appl Energy 1990;37:169–87.

[29] Zhang J, Yuan J, Yuan H. Numerical and experimental investigation of phase change characteristics and desalination effect of seawater freezing desalination in narrow channels. Desalination 2022;544:116145.

[30] Faizal M, Ahmed MR. Experimental studies on a closed cycle demonstration OTEC plant working on small temperature difference. Renew Energy 2013;51:234–40.

[31] Aydin H, Lee H-S, Kim H-J, Shin SK, Park K. Off-design performance analysis of a closed-cycle ocean thermal energy conversion system with solar thermal preheating and superheating. Renew Energy 2014;72:154–63.

[32] Vera D, Baccioli A, Jurado F, Desideri U. Modeling and optimization of an ocean thermal energy conversion system for remote islands electrification. Renew Energy 2020;162:1399–414.

[33] Hasan A, Dincer I. A new integrated ocean thermal energy conversion-based trigeneration system for sustainable communities. J Energy Res Technol 2020;142: 061301.

[34] Takleh HR, Zare V. Employing thermoelectric generator and booster compressor for performance improvement of a geothermal driven combined power and ejector-refrigeration cycle. Energ Conver Manage 2019;186:120–30.

[35] Zhou S, Liu X, Bian Y, Shen S. Energy, exergy and exergoeconomic analysis of a combined cooling, desalination and power system. Energ Conver Manage 2020; 218:113006.

[36] Tang Z, Wu C, Liu C, Xu X, Liu J. Thermodynamic analysis and comparison of a novel dual-ejector based organic flash combined power and refrigeration cycle driven by the low-grade heat source. Energ Conver Manage 2021;239:114205.

[37] Que H, Chen C-C. Thermodynamic modeling of the NH3–CO2–H2O system with electrolyte NRTL model. Ind Eng Chem Res 2011;50:11406–21.

[38] Crowe CT, Schwarzkopf JD, Sommerfeld M, Tsuji Y. Multiphase flows with droplets and particles. CRC Press; 2011.

[39] Hsu C-T-A, Shih S-M. Semiempirical equation for liquid-phase mass-transfer coefficient for drops. AIChE J 1993;39:1090–2.

[40] Kolev NI, Drag forces, Multiphase Flow Dynamics 2: Thermal Mechanical Interactions, (2005) 27-60.

[41] Churchill SW. Comprehensive correlating equations for heat, mass and momentum transfer in fully developed flow in smooth tubes. Ind Eng Chem Fundam 1977;16: 109–16.